ETH
Eidgenössische Technische Hochschule Zürich
Swiss Federal Institute of Technology Zurich

Alpine pumping and its role for summer precipitation

MASTER THESIS

SWISS FEDERAL INSTITUTE OF TECHNOLOGY ZÜRICH (ETHZ)
INSTITUTE FOR ATMOSPHERIC AND CLIMATE SCIENCE (IAC)

Author:
Susanne BIERI
sbieri@student.ethz.ch

Supervisors:
Wolfgang LANGHANS
Dr. Jürg SCHMIDLI
Prof. Christoph SCHÄR

March 2011

Contents

List of Figures

Abstract

Differential heating between Alpine valleys and the adjacent foreland induces a complex and multi-scale system of mass, heat, and moisture transport. The formation of up-valley (daytime) and down-valley (nighttime) wind-systems is frequently observed during flat-pressure distributions in summer and commonly abbreviated as Alpine pumping. This plain-to-mountain circulation induces horizontal convergence which is expected to be compensated by vertical motions. But different studies have recently been suggested that the initiation of deep orographic convection can not directly be related to this horizontal wind field and the link between moist convection and Alpine pumping is still a controversial issue.

The aim of this study is to quantify Alpine pumping and its interaction with convection for one particular summer-month, which revealed pronounced thermally-driven Alpine circulations. For this purpose, surface-based and remote-sensing observational data are compared to convection-permitting numerical simulations (CRMs). The latter are conducted with the mesoscale model COSMO and differ in their horizontal resolution ((O(1 km) and O(2 km)). However, since resolution and parameterization requirements for kilometer-scale simulations are partly unclear, the involved physics and dynamics of the simulated Alpine pumping have initially been validated in detail against the observations.

In a valley based validation the CRMs are capable to represent the diurnal evolution of surface radiation, horizontal pressure graident, anabatic wind, and precipitation. The difference between the two CRMs is small meaning little impact of increased horizontal grid-spacing on the overall evolution of Alpine pumping and the formation of precipitation. Compared to a convection-parameterizing simulation (O(6 km)), the CRMs realise a more accurate (later) onset of deep convection but still show deficits in adequately simulate the transition between shallow and deep convection and nighttime cloudiness. Also, the surface radiation budgets during the morning and evening transition periods differ from the observations, as topographic shading of incoming radiation has not yet been taken into account.

With a validation of a larger plain-to-mountain perspective convergence in the Alpine region is found to peak slightly before deep convection is strongest, and ends soon after the diurnal precipitation maximum is reached. This could suggest a favoring of orographic convection due to the prevailing convergence and a transition to divergent flow due to cold-air outflow soon after the convection.

Zusammenfassung

Unterschiedliche Erwärmung zwischen Alpentälern und dem Vorland induzieren ein komplexes System aus Masse-, Wärme- und Feuchtetransport. Die Entstehung von Talwind (während des Tages) und Bergwind (während der Nacht) wird meist unter flachen Druckverteilungen im Sommer beobachtet und ist in der alpinen Region unter 'Alpine pumping' bekannt. Diese Windzirkulation verursacht eine Massenkonvergenz über den Alpen, welche aufgrund von Massenerhaltung durch vertikale Bewegungen kompensiert werden müssen. Allerdings haben verschiedene Studien angedeutet, dass die Enstehung von tiefer Konvektion über den Alpen nicht direkt mit diesem horizontalen Windfeld verknüpfbar ist. Der Zusammenhang zwischen tiefer Konvektion und 'Alpine pumping' ist immer noch umstritten.
Das Ziel dieser Arbeit ist es 'Alpine pumping' und dessen Interaktion mit Konvektion für einen speziellen Sommermonat zu quantifizieren. Dazu werden convection-permitting Simulationen (CRMs) mit Beobachtungen verglichen. Die Simulationen stammen von dem COSMO Modell und unterscheiden sich in ihrer horizontaler Auflösung (O(1 km), O(2 km)).
Eine talbasierte Auswertung zeigt, dass die CRMs fähig sind den Tagesgang von Oberflächenstrahlung, horizontalem Druckgradienten, anabatischem Wind und Niederschlägen ausreichend darzustellen. Der Unterschied zwischen den beiden CRMs ist klein, was auf einen geringen Einfluss von erhöhtem horizontalem Gitterabstand auf die Simulation von 'Alpine pumping' und konvektiver Niederschläge hindeutet. Die CRMs zeigen im Gegensatz zu einer O(6 km)-Simulation mit Konvektionsparametrisierung, einen präzisen Beginn von tiefer Konvektion. Alle Simulationen zeigen Defizite in der Modellierung von flacher Konvektion wie auch im nächtlichen Bewölkungsgrad. Zusätzlich wird die Oberflächenstrahlung in den CRMs während Sonnenaufgang und Sonnenuntergang überschätzt, was auf die Vernachlässigung der Abschattung der Gebirge zurückzuführen ist.
Anhand einer Validierung einer grösser-skaligen Perspektive zeigt sich, dass das Maximum der Konvergenz kurz vor dem Maximum der tiefen Konvektion erreicht wird. Der Wechsel zur Divergenz geht einher mit dem Tagesmaximum der Niederschläge. Dies deutet darauf hin, dass eine Unterstützung der Konvektion über den Alpen durch die Massenkonvergenz möglich ist.

1. Introduction

1.1. Motivation

In today's context of global warming (e.g. forth assessment report of the Intergovernmental Panel on Climate Change by Solomon et al. (2007)) the impacts on rising global temperature are multiple. Several studies (see e.g. Frei et al., 2006, Christensen and Christensen, 2003) showed the severe changes in the hydrological cycle over Europe as a result of the increased air temperatures. Overall the summer precipitation will be reduced in many midlatitude regions (Christensen and Christensen, 2003) with increasing summertime precipitation extremes (Frei et al., 2006, Christensen and Christensen, 2003). Modelling studies further showed (Frei et al., 2006) that large model differences occur especially in simulating summertime precipitation.

With today's computer capabilities it is possible to reduce the grid spacing of regional climate models to a few kilometres. These convection-permitting models are especially beneficial in the Alpine region, which is a challenging region to model due to the highly complex terrain. With reduced grid spacing a better representation of surface fields and topography can be realized in numerical models. Additionally, deep convection can be explicitly resolved instead of being parameterized.
Several studies (e.g. Hohenegger et al., 2008, Steppler et al., 2003) showed that with this explicit treatment of convection, small-scale features can be modelled more accurately and realistically, and that diurnal cycles of precipitation are better captured. Convection-permitting models are a benefit for such modelling scenarios and could therefore improve the simulation of summertime precipitation (see e.g. Hohenegger et al., 2008) and hence be a chance in a correct simulation of the hydrological cycle in a changing climate. However, the case study by Trentmann et al. (2009) showed that simulating local convection is still a challenging test with convection-permitting models. Further, Bryan et al. (2003) questioned from a turbulence modellers perspective, whether O(1 km) is enough of explicitly resolve deep convection.

The dominant form of summer precipitation over the Alps is convective precipitation (Frei and Schär, 1998). Summertime flat-pressure distributions over the Alps favour the evolution of localized thunderstorms and convective precipitation due to the absence of subsidence (Ahrens, 1994). The strong insolation during these 'fair-weather' days conclude in a differential heating in mountainous terrain. The air within valleys is heated faster than the air over an adjacent plain (Steinacker, 1984) leading to a pressure difference between the mountain (valleys) and the adjacent plain (Whiteman, 1990). This pressure difference drives a thermal circulation pointing towards (away from) the mountain during the day (night). In the Alpine region this dynamical process is called Alpine pumping proposed by Lugauer and Winkler (2005). In consequence of this plain-to-mountain circulation mass is advected to the mountains leading to a positive mass convergence over the mountains. With this positive mass convergence ascending is expected over the mountains due to mass conservation (e.g. Geerts et al., 2008).
Analysis of observations during the Mesoscale Alpine Programme (MAP) in the Riviera valley showed that this thermally induced cross-valley circulation transfers heat and moisture from close to the surface to upper levels (Rotach and Zardi, 2007). This might be linked to the formation of convective clouds and convective precipitation over highly complex terrain or rather sustain orographic convection and precipitation (Geerts et al., 2008). A schematic representation of the thermally forced circulation is showed in Fig. 1.1. However, the link between convergence and formation of deep convection is less understood and under investigation (e.g. Demko et al., 2009, Demko and Geerts, 2010)). With nowaday's computer

capabilites and convection-permitting models it is possible to investigate this interaction between the mass convergence, the following ascending air over mountains and the formation of convection.

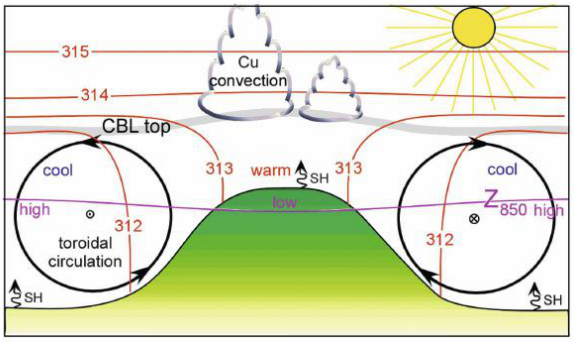

Figure 1.1.: Schematic representation of the thermally forced circulation over an isolated heated mountain (isentropes (red lines), one isobar (purple line, height of the 850-mb surface, therefore the direction of the pressure gradient), convective boundary layer top) from Geerts et al. (2008)

This study aim to investigate the representation of Alpine pumping of model simulations with different horizontal resolutions using observational data and to evaluate the overall interaction of Alpine pumping on convective precipitation over the Alps. The model runs were conducted with the COSMO (COnsortium for Small-scale MOdelling) model which is also used for operational forecasting at the Swiss Weather Service MeteoSwiss. The conducted model runs were compared to observations with respect to the process Alpine pumping and the interaction on convective precipitation. The different model runs vary in their horizontal resolution (O(1 km), O(2 km) and O(6 km)).

1.2. Goals and outline of the thesis

The aim of this thesis is to quantify the observed and modelled thermally induced plain-to-mountain circulation, Alpine pumping, and to investigate the link with convective precipitation over the Alps. For that purpose, numerical simulations with convection-permitting resolutions are conducted and compared against observations.

Specific research questions that are addressed in this thesis are:

- Does the simulated Alpine pumping and moist convection agree with observations?
- What is the impact of horizontal grid resolution on the simulation of Alpine pumping and moist convection?
- Is there a link between Alpine pumping and summer precipitation?
- What demands does the accurate simulation of Alpine pumping make of regional climate models - especially in resolution?

The outline of this thesis is as following: In chapter 4 the locally induced Alpine pumping in different Alpine valleys is investigated mostly using surface observations. Then an Alpine polygon is defined in chapter 5 to get an understanding of the overall interaction between the plain-to-mountain circulation and convective precipitation. Further, in chapter 6, modelling sensitivities are conducted. Finally, the discussion and conclusion is made in chapter 7.

2. Theory

2.1. Alpine pumping

Over mountainous terrain a thermally induced wind system evolves due to differntial heating. Figure 2.1 shows the schematic diagram of Defant (1949). A diurnal cycle of circulation develops because of a horizontal pressure gradient due to a temperature difference between the air in the valley and the air over the adjacent plain (Whiteman, 1990). The same terminology as in Whiteman (1990) is used in this thesis, which is indicated in Fig. 2.1 in italics. Slope winds blow parallel to the inclination of the slope driven by buoyancy forces due to a temperature difference between the air adjacent to the slope and the air outside the slope. However, valley winds blow parallel to the longitudinal axis of a valley forced by a horizontal pressure gradient (Whiteman, 1990). During the course of a day, up-slope winds develop (see Fig. 2.1 A, B), transition from down-valley winds (night, Fig. 2.1 H, A) to up-valley winds (day, Fig. 2.1 C, D) occurs, and up-slope winds cease and reverse to down-slope winds after sunset (Fig. 2.1 E, F). Regarding this thesis the focus was layed on the valley-wind system.

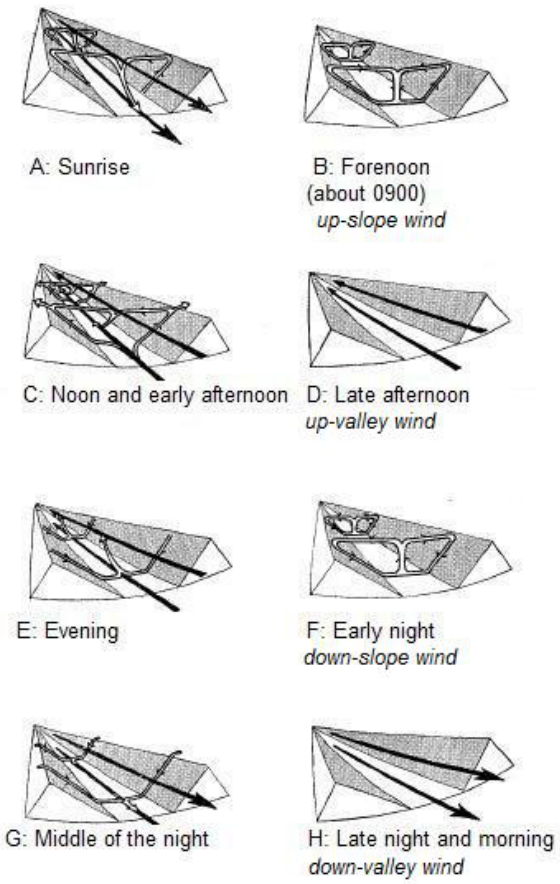

Figure 2.1.: Diurnal cycle of valley winds (after Defant (1949), terminology adapted from Whiteman (1990))

For the previously described complex series of processes the term Alpine pumping is proposed by Lugauer and Winkler (2005) and is used in this thesis synonymous for thermally induced wind systems.

The reason for the strong difference in temperature between the valley and the plain was subject of several studies (e.g. Defant, 1949, Whiteman, 1990, Rampanelli et al., 2004, Schmidli and Rotunno, 2010). A common explanation is the valley volume effect (Steinacker, 1984). From the first and second laws of thermodynamics follows the smaller the volume, the larger the potential temperature change for the same heat increment Q. This relation can be expressed as $Q = \rho c_p V(T/\theta) d\theta$, where ρ is the air density, c_p the specific heat, V the volume, $d\theta$ the potential temperature change and (T/θ) the ratio of actual to potential temperature (Whiteman, 1990).

As the valley atmosphere is smaller than the plain atmosphere, the temperature change for the same heat increment is larger over the valley during the day and reversed during the night. This concept can be quantified by using a topographic amplification factor (TAF),

$$\tau = \frac{\frac{A_{xy}(h)}{V_{valley}}}{\frac{A_{xy}(h)}{V_{plain}}} \tag{2.1}$$

where $A_{xy}(h)$ is the horizontal area through which energy enters and h is the height above the valley floor or plain (Whiteman, 1990). $V = h \cdot A_{xy}(h)$ is the underlying valley or plain volume, respectively (Steinacker, 1984).
Therefore, with the help of equation of state and conservation of mass (see equation (2.2), where p is the pressure, z the height above surface, R the gas constant, T the temperature and g the gravitational acceleration), it follows that a warmer (cooler) column will have a lower (higher) pressure at each height, producing an along-valley pressure gradient which further induces an acceleration producing an up-valley (down-valley) wind (Whiteman, 1990).

$$\frac{dp}{p} = -\frac{gdz}{RT} \tag{2.2}$$

However, studies (e.g. Rampanelli et al., 2004, Schmidli and Rotunno, 2010) showed limitations of the TAF concept. The main underlying assumption of TAF is that no heat exchange through the valley top occurs (Schmidli and Rotunno, 2010). The valley-volume effect was questioned by Rampanelli et al. (2004) who observed compensating subsidence in the valley center which contributes to the heating in the valley center. Schmidli and Rotunno (2010) showed further, with a new diagnostic framework, that the TAF concept can qualitatively be used as an explanation of the along-valley wind. However, Schmidli and Rotunno (2010) disprove the basic assumption of no heat exchange through the valley top. Further, eventhough there exists a local heating in the valley core due to compensating subsidence, the net effect of the slope-flow circulation results in a heating loss. This cross-valley circulation leads to a negative heat budget, less heatinggggggg and therefore less drive for valley winds (Schmidli and Rotunno, 2010).

Qualitatively, Alpine pumping evolves through a temperature difference between a valley and a plain. This temperature difference leads to a pressure gradient driving the thermal circulation. A theory for the computation of the horizontal pressure differences is proposed by Geerts et al. (2008). In their calculations they are thinking of pressure perturbations instead of only reduced station pressure. This procedure is proposed by Geerts et al. (2008) because it is not as sensitive to different stations altitude as only hydrostatic reduction would be. The approach by Geerts et al. (2008) is used in this thesis: As perturbations are departures from a 'mean' state the pressure has firstly been removed from the 24-h station mean value $\overline{p}_t$. This leads to the so-called single pressure perturbations p'. Further, $\overline{p}_s$, the mean of $\overline{p}_t$ for all stations at given time, is removed to account for diurnal pressure variations. This gives the so-called double pressure perturbations p''. Geerts et al. (2008) showed further, that if treatening the

finite difference as a differential and assuming hydrostatic balance the double pressure perturbation p'' can be expressed as a measure for horizontal pressure gradient ($\frac{\delta p}{\delta r}$). This gives the equation

$$\frac{\Delta p''}{\Delta r} = \frac{\delta p}{\delta r} - (\rho - \overline{\rho}_t) g \frac{\Delta z}{\Delta r}, \tag{2.3}$$

where ρ is the air density and $\overline{\rho}_t$ the 24-h mean air density (Geerts et al., 2008). With the help of the ideal gas law and remarking that ($\frac{\Delta z}{\Delta r}$) is the average slope S of the terrain, equation (2.3) becomes

$$\frac{\delta p}{\delta r} = \frac{\Delta p''}{\Delta r} + (p - \overline{p}_t) g \frac{\rho}{p} S - (T_v - \overline{T_v}) g \frac{\rho}{T v} S \tag{2.4}$$

Here T_v is the virtual temperature, $\overline{T}_v$ the mean virtual temperature and g the gravitational acceleration (Geerts et al., 2008).

2.2. Alpine-scale mass convergence

As a consequence of this plain-to-mountain circulation mass is advected to the mountains leading to a positive mass convergence over the mountains. Different studies were conducted in the Santa Catalina Mountains in southeast Arizona to study the mountain-scale surface convergence and thermal forcing (e.g. Geerts et al., 2008, Demko et al., 2009). The Santa Catalina Mountains are isolated and typically reveal strong thermally induced circulations.
The conceptual view of the interaction between this circulation and the evolution of convection is acquired from Geerts et al. (2008) and is declared in Fig. 1.1. The toroidal circulation leads to a horizontal mass convergence towards the mountain which thereafter sustains the cumulus convection over the mountain (Geerts et al., 2008). Follow-up studies (e.g. Demko et al., 2009, Demko and Geerts, 2010) showed further that on one hand thunderstorms over orographic terrain suppress the near-surface convergence due to cold-pool formation. On the other hand they showed that mass convergence may sustain orographic convection but not explain the initation of deep convection. Demko and Geerts (2010) revealed further that the onset of orographic convection comes from local surface heating than initated from mass convergence.

In the Alpine region the prevailing form of summertime precipitation is convective precipitation (Frei and Schär, 1998). As for the Santa Catalina Mountains an interaction of plain-to-mountain flow and convection might be an explanation for the Alpine region. Hence the Alpine arc can be viewed as isolated 'mountain' and the large-scale plain-to-mountain circulation can be regarded as toroidal circulation sustaining convection and thereafter precipitation. For an investigation of the interaction between orographic flow and precipitation in this specific case of the Alps the mass convergence for an Alpine polygon was calculated.

Demko et al. (2009) describes the mass convergence (MC, kg m^{-1} s^{-1}) as

$$MC = \oint \rho v_n ds, \tag{2.5}$$

where v_n describes the wind component normal to the track, ds the incremental distance along the line integral. As a sign convention v_n is positive blowing up-valley and negative blowing down-valley.
With the divergence theorem the mean convergence (s^{-1}) can be written as

$$A^{-1} \oint v_n ds = -\vec{\nabla} \cdot \vec{v_h} \tag{2.6}$$

where $\vec{v_h}$ denotes the horizontal wind vector.

As in Geerts et al. (2008) this formula can be rewritten to become

$$-\vec{\bigtriangledown} \cdot \vec{v_h} = A^{-1} \oint v_n ds = \frac{\overline{v_n} C}{A} \tag{2.7}$$

where $\overline{v_n}$ is the 24h-mean inflow (anabatic wind speed), A the the area and C the loop length of a polygon. Equations (2.5) and (2.6) lead to equation (2.8) which is the mean convergence normalized by the area. This mass convergence is used in this thesis.

$$MC = \oint \rho v_n ds = -A \vec{\bigtriangledown} \cdot \rho \vec{v_h} \tag{2.8}$$

3. Method

3.1. Validation process

The validation of Alpine pumping and its interaction with convective precipitation can be seperated in two different scales. On one side Alpine pumping consists of valley-winds which take place on a smaller mesoscale. On the other side the large plain-to-mountain circulation as a whole appears on a larger mesoscale. For these different processes and their scales two different validations were considered:

1. Valley-scale validation: Surface measurements (pressure, temperature, wind) are analysed from valley and plain stations in the Alpine region in order to see the evolution of Alpine pumping. For the field data (precipitation data) mainly Switzerland was investigated. The observational data is compared to model data.

2. Alpine-scale validation: Satellite and model data are studied at a larger scale using an Alpine polygon in order to consider further the influence of mass convergence and initation of convection on a plain-mountain perspective. On this larger scale only satellite data is available for a comparison with model data.

3.1.1. Valley-scale validation

Stations at six valley-plain pairs were selected in the Alpine region. A description of these stations is given in Table 3.1 and their location is shown in Fig. 3.2. The selection was chosen on purpose of available data and feasibility of a station. The stations have also be chosen because valley-wind or mountain-plain circulations are well documented (see e.g. Lugauer et al., 2003, Lugauer and Winkler, 2005, Weissmann et al., 2005). For the horizontal pressure difference a plain station for each valley station is selected. The plain station is chosen with a sufficient distance to the valley station and a ideal location in the plain. The valley orientation was examined using geographical maps and information was obtained from MeteoSwiss. Further, gridded precipitation observation was examined mainly over Switzerland.

The disadvantages of this model validation are the limit of stations available and the limitation to the surface. The advantage is the direct comparison with observations.

Valley name	*valley station*	*plain station*	*distance between the two stations*	*valley orientation*	*rotation angle*
Rhine valley	Chur	St.Gallen	64 km	NE-SW	30°
Rhone valley	Sion	Bern-Liebefeld	79 km	W-E	90°
Aare valley	Interlaken	Wynau	109 km	W-E	90°
Reuss valley	Altdorf	Basel	67 km	NW-SW	315°
Inn valley	Innsbruck	Munich	101 km	W-E	90°
Loisach valley	Garmisch	Munich	85 km	NE-SW	30°

Table 3.1.: Characteristics of six selected valleys with their corresponding valley and plain stations, respectively.

3.1.2. Alpine-scale validation

For a larger plain-mountain perspective an Alpine-scale validation was chosen which allows to see the whole interaction of Alpine pumping and convection/precipitation concerning this Alpine polygon. Unfortunately these results can not be compared to surface observations but only to satellite data. Figure 3.1 shows the topography and the Alpine polygon used in each model run. For a selection of the Alpine polygon the topography was filtered with a sharp spectral cut-off at λ=183 km and then afterwards the 700 m isoline was chosen to be the distinction of the Alpine polygon (each marked in Fig. 3.1). In Fig. 3.1 also the different representation of the topography in the three different model runs is visible.

The advantage of this validation is the oppurtunity to see the interaction between the horizontal (in horizontal mass convergence) and the vertical flow (as a result in precipitation). Additionally the predictability for a larger area is higher. On contrary no surface observations are available for a direct comparison for this large area. But satellite data can be used for a comparison of this large plain-mountain perspective.

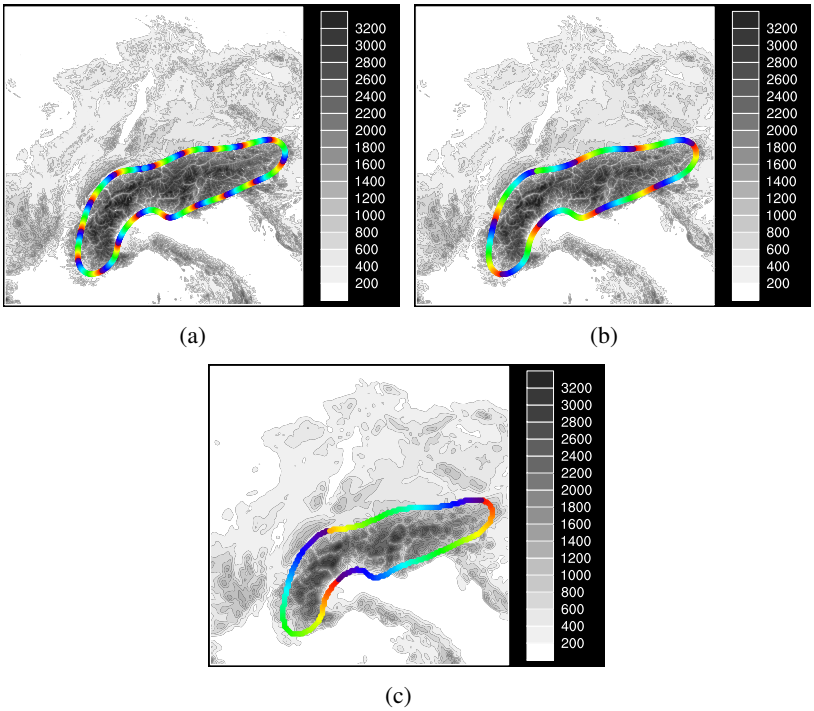

Figure 3.1.: Topography (m) of the model domain at three different model gridspacings (a) SU1, (b) SU2 and (c) SU7. The contour line indicates the arc studied by the Alpine-scale validation.

3.2. Observational data

For the validation part the numerical model is compared against different observational datasets. The datasets are provided by the Swiss Weather Service MeteoSwiss, the Alpine Surface Radiation Budget (ASRB) network (Marty et al., 2002) and EUMETSAT.

3.2.1. Surface measurements of standard atmospheric parameters

The ANETZ data is provided by MeteoSwiss and comprises data at a resolution of 10 minutes with the exception of wind speed, which is only hourly available. Further, hourly SYNOP data is provided

from MeteoSwiss. From this dataset 11 stations have been selected which are located either within a pronounced valley or outside in a corresponding plain (see Table 3.2). Figure 3.2 shows the geographical location of these stations. Eight are located in Switzerland, one in Austria and two in Germany. Following parameters were used in the analysis: 2m-temperature, 2m-dew point temperature, pressure at station height, wind direction and scalar wind speed at 10 m above surface.

name (dataset)	*longitude*	*latitude*	*height*	*corresponding valley/plain counterpart*	*abbreviation in Fig. 3.2*
Chur (ANETZ)	9.53E	46.86N	556 m	St.Gallen	CHU
St.Gallen (ANETZ)	9.40E	47.43N	779 m	Chur	STG
Sion (ANETZ)	7.33E	46.22N	482 m	Bern-Liebefeld	SIO
Bern-Liebefeld (ANETZ)	7.42E	46.93N	565 m	Sion	BER
Interlaken (ANETZ)	7.87E	46.67N	577 m	Wynau	INT
Wynau (ANETZ)	7.78E	47.25N	422 m	Interlaken	WYN
Altdorf (ANETZ)	8.63E	46.86N	449 m	Basel	ALT
Basel (ANETZ)	7.58E	47.53N	316 m	Altdorf	BAS
Innsbruck (SYNOP)	11.35E	47.27N	584 m	Munich	INN
Garmisch (SYNOP)	11.07E	47.48N	720 m	Munich	GAR
Munich (SYNOP)	11.55E	48.17N	526 m	Innsbruck/Garmisch	MUN
Davos (ASRB)	9.85E	46.81N	1610 m	-	DAV
Cimetta (ASRB)	8.8E	46.20N	1670 m	-	CIM
Versuchsfeld SLF (ASRB)	9.82E	46.83N	2540 m	-	SLF

Table 3.2.: Used stations in the valley-scale validation part (11 stations for standard atmospheric parameters and 3 stations for radiation data), their geographical location and their corresponding counterpart for the pressure difference.

3.2.2. Radiation measurements

The radiation dataset used in this study was provided from the ASRB network (Marty et al., 2002). The ASRB is part of the Swiss Atmospheric Radiation Monitoring Program, which aims at studying the radiation budget in the Alps (Marty et al., 2002). In total eleven stations are involved in the ASRB network and are measuring downward short- and longwave radiative fluxes. Some of these stations are also equipped with instruments measuring emitted longwave and reflected shortwave radiation. The data output is half-hourly. At fully equipped stations (Davos, Cimetta, and Versuchsfeld SLF, see Table 3.2) it is possible to analyse the full radiation budget.
For the radiation budget all incoming fluxes (shortwave incoming SWin and longwave outgoing LWout) were defined positive and the outgoing ones (shortwave outgoing SWout and longwave outgoing LWout) as negative.

3.2.3. Precipitation measurements

For the validation of precipitation two different datasets were available. Firstly, radar observations (RAD) that cover Switzerland and parts of neighbouring countries were used. The radar images have been composed from three C-band radars located on the top of La Dôle, Albis and Monte Lema (Germann et al., 2006), respectively, provided by MeteoSwiss. The radar reflectivity Z (mm^6 m^{-3}) has been transformed into rain rate R (mm h^{-1}) with an empirical Z-R relation Z=316R$^{1.5}$. Secondly, a dataset that combines daily surface observations from gauge measurements in Switzerland with radar observations (DES_GAUGE) has been provided by MeteoSwiss. This gridded dataset is available only over Switzerland and maximizes the advantages of both individual datasets (e.g. comparatively accurate gauge measurements and high spatiotemporal resolution of the radar (Wüest et al., 2009)).

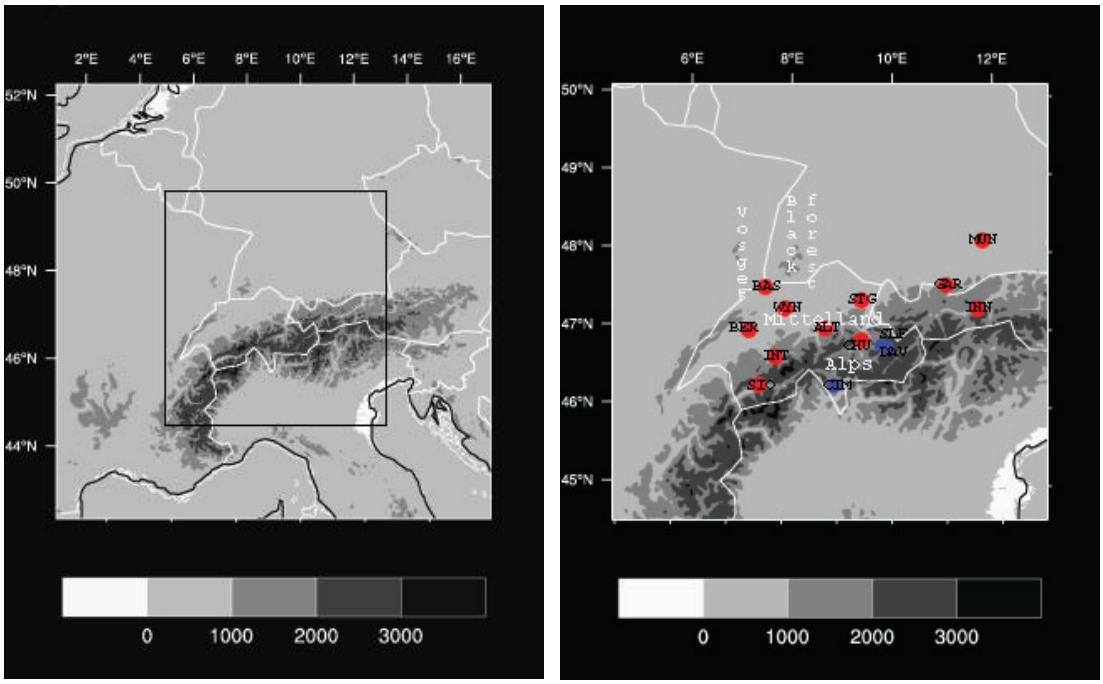

(a) (b)

Figure 3.2.: (a) Model domain and topography (m) for 2-km model run. The black box indicates the zoom for (b) geographical location of the used stations (red: ANETZ/SYNOP stations and blue: ASRB stations) with their abbreviations used in Table 3.2. In white the distinct geographical regions used in this thesis are indicated.

3.2.4. Satellite data

Further, satellite data provided by EUMETSAT was used. In this study the Meteosat Second Generation Satellite Meteosat 8 is used with a horizontal resolution of about 3 km (Schmetz et al., 2002). On one hand the infrared window channel is used (IR108, 10.8 μm) which shows the cloud amount in the troposphere. On the other hand, the water vapour absorption band is applied (WV67, 6.7 μm) for the detection of overshooting tops.

Overshooting tops exist in deep convective storms where the updraft is of sufficient strength to penetrate through the tropopause (Bedka et al., 2010). These overshooting tops can be investigated using global satellite observations (e.g. Ackermann, 1996, Schmetz et al., 1997). Normally, the 10.8 μm brightness temperature (BT) is larger than the 6.7 μm BT because the surface is usually warmer than the upper troposphere (Ackermann, 1996). However, global satellite observations observed that for cold cloud tops the 6.7 μm BT can be larger than the 10.8 μm BT (Schmetz et al., 1997). Through the overshooting storm updraft water vapour is forced into the lower stratosphere. Since the temperature increases with height in the stratosphere this water vapour emits in warmer temperature. However, the 10.8 μm BT originates from the colder physical cloud top which is located at the colder tropopause (Bedka et al., 2010). Hence, for deep convective storms the 6.7 μm BT can be larger than the 10.8 μm BT (Bedka et al., 2010). This knowledge can be used for the detection of deep convection.

3.3. Numerical model

For the process validation the numerical COSMO model version 4.12 is used. The COSMO model is a nonhydrostatic limited-area model developed originally by the German Weather Service (Steppler et al., 2003). For a detailed model description see Langhans et al. (2011).

3.3.1. Model description

The simulated domain covers a large Alpine Region of 1100 x 1100 km (see Fig. 3.2a). The domain contains from 166 by 166 to 500 by 500 up to 1000 by 1000 grid points in the horizontal and 46 atmospheric levels in the vertical. In the vertical a pressure-based hybrid coordinate is used. The dynamics are based on a split-explicit 3rd-order Runge-Kutta scheme (Doms and Förstner, 2004). Initial and lateral boundary conditions are supplied by the operational analysis of the European Centre for Medium Range Weather Forecasts (ECMWF). A prognostic TKE-based scheme with a closure on level 2.5 (Raschendorfer, 2001) is used to describe the vertical turbulent diffusion. For the horizontal diffusion a 2D-Smagorinsky scheme is used (Smagorinsky, 1963) and diffusion is computed along model levels. In all model runs no computational mixing was used. If not mentioned differently, the aerosol climatology of Tanré et al. (1984) was used within the radiative flux computation. Topographic shading has not been taken into account in these simulations.

In total seven different model runs were conducted (see Table 3.3). Three of these runs are the focus of model validation. The other four runs (_AER and _LEXPCOR) are sensitivity experiments. Table 3.3 summarises specific setups of the simulations. For convenience the three model runs were named SU1, SU2 and SU7 according to their corresponding horizontal resolutions in kilometres. The _AER is added if the new aerosol climatology after Tegen et al. (1997) is used, wheras the _LEXPCOR is added if only the namelist switch to lexpcor=.False. is done. In the figures the model runs are named SU1_SMAG2D_M, SU2_SMAG2D_M and SU7_SMAG2D_M, respectively, but corresponds to SU1, SU2 and SU7 called in the thesis, respectively.

This differing horizontal resolution has two important impacts:

- The two finer model runs (O(1 km) and O(2 km)) do not have a parameterization scheme for convection, implying that convection should be explicitly resolved in these model runs. On the contrary the coarser model run (O(6 km)) uses a parameterization scheme after Tiedtke (1989). The comparison between these model runs shows the direct effect of explicit resolution of convection and hence the benefit of convection-permitting models.

- The model runs differ with their representation of the topography and hence the representation of the complex terrain of the Alps. Table A in Appendix shows the different areas for the Alpine polygon (see section 3.1.2). The varied areas differ from $1.54*10^4$ km^3 in O(1 km) model run to $1.12*10^4$ km^3 in O(6 km) model run with a z-top=1000m. This differing areas have a direct effect on the heat increment in the valley (see equation (2.1)) and therefore on the evolution of thermally induced valley-wind systems and the overall plain-to-mountain circulation. Hence the convection-permitting models should show a better abstraction of Alpine pumping and the physical feedback to convective precipitation.

3.3.2. Integration

Simulations are performed for a period of one month, July 2006. This is the same period as studied by Hohenegger et al. (2008). In this period the weather pattern in the Alpine region was characterized by a predominant flat pressure distribution interrupted by two advective periods. Over many parts of the simulated domain, July 2006 was the warmest July since systematic data record 1864 (MeteoSchweiz,

2006) and with a flat pressure distribution it makes this month favourable for the evolution of Alpine pumping and a great likelihood for convective development. Only at the beginning and the end of the month a frontal passage provided some more precipitation (Hohenegger et al. (2008)). For these synoptic reasons the period was subdivided into two analysis sections:

- 0600 UTC 01 July 2006 until 0600 UTC 31 July 2006: whole month, neglecting the first six hours of model spin up.
- 0000 UTC 09 July 2006 until 0000 UTC 27 July 2006: without the impact of frontal systems which occurs in the beginning and at the end of July 2006 (weak synoptic forcing period). These period is characterized with fair-weather conditions and thus well developed thermally-driven flows.

Modeloutput interval is 30 minutes.

Model run	*Grid point spacing*	*# hor.grid points*	Δt	*lexpcor*	*Cloud-permitting model*	*Aerosol climatology*
SU1	0.01°	1000 x 1000	6s	.True.	yes	after Tanré et al. (1984)
SU2	0.02°	500 x 500	15s	.True.	yes	after Tanré et al. (1984)
SU7	0.06°	166 x 166	60s	.False.	no	after Tanré et al. (1984)
SU1_LEXPCOR	0.01°	1000 x 1000	6s	.False.	yes	after Tanré et al. (1984)
SU2_LEXPCOR	0.02°	500 x 500	15s	.False.	yes	after Tanré et al. (1984)
SU1_AER	0.01°	1000 x 1000	6s	.False.	yes	after Tegen et al. (1997)
SU2_AER	0.02°	500 x 500	15s	.False.	yes	after Tegen et al. (1997)

Table 3.3.: The characteristics of firstly, the three used model runs which play major part in the validation process and secondly the four model runs with two modifications for a modelling sensitivity study: Firstly, a namelist switch to lexpcor=.False. (_LEXPCOR) and secondly, a new aerosol climatology (_AER) after Tegen et al. (1997).

3.3.3. Synthetic observations

As described in section 3.1, firstly, the above selected stations were compared to each model run. The model output was interpolated using inverse distance weightning. A comparison with a nearest-neighbour interpolation showed that the interpolation method does not influence the results. For the comparison synthetic observations were calculated including the horizontal pressure difference (as described in section 2.2) between two stations, potential temperature, and radiative fluxes.

The advantage of this method is the opportunity of a direct comparison with observations. The disadvantages are clearly the limited station numbers and sometimes the unrepresentative station location.

Supplementary to the surface measurements remote sensing data was used. Especially, for the onset (timing and location) of convection satellite pictures are a benefit.

Synthetic satellite images were calculated online from the COSMO forecasts. The calculation uses the fast radiative transfer model for TIROS Operational Vertical Sounder (RTTOV). RTTOV calculates the BT from a given atmospheric profile of temperature, variable gas concentrations, cloud and surface properties and is a diagnostic tool in the COSMO model (Keil et al., 2006). Uncertainties related to this method are also outlined by Keil et al. (2006).

For a validation of different cloud types the BT was linked to cloud types as in Keil et al. (2006). These here used cloud types are listed in Table 3.4. The corresponding heights are estimated using radiosoundings (see Appendix Fig. H.1). These heights are roughly the same heights for clouds used in synoptic weather classification (Ahrens, 1994).

used 'cloud name'	*corresponding BT temperature*	*approximate height*
cloud-free and low cloudiness regions	BT > 0°C	surface - 4000 m
mostly 'mid-level' clouds	-20°C < BT < 0°C	4000 m - 7000 m
mostly 'high' clouds	BT < -20°C	from 7000 m

Table 3.4.: Used names of clouds concerning their BT as in Keil et al. (2006) and their approximate height estimated from radiosoundings (see Appendix Fig. H.1).

For the following discussion specific names are introduced here for distinct geographical regions, which are indicated in Fig. 3.2.

4. Valley-scale validation

For the valley-scale validation the different parameters available in the observations were compared to three different model runs. In the remainder of this thesis, time will be given in UTC, which is two hours less than local time. If not explicitly mentioned the whole month July 2006 was analysed.
Due to the different horizontal resolutions of the model runs the topography is differently resolved. Table A in Appendix shows the different valley-volume for the different model runs and varying top level. The valley-volume is as larger as smaller the horizontal resolution of a model simulations gets and surely has implications on the simulations of the different parameters.

4.1. Wind speed and wind direction

A first insight into the phenomena of Alpine pumping is given by the surface wind measurements. As described in section 2, down-valley wind can be observed during night and up-valley wind during the day (Whiteman, 1990). For each of the selected six valley stations the anabatic up-valley wind was calculated from 10-m wind. The rotation angles used are listed in Table 3.2. Figure 4.1a shows the mean diurnal cycle of the anabatic wind from simulations and observations averaged over the six valleys and over the whole month.
The diurnal change from anabatic wind (during day, up-valley) and katabatic wind (during night, down-valley) is visible in the observations. The anabatic wind during the day is stronger compared to the katabatic wind and peaks around 1300 UTC. This stronger anabatic wind follows the stronger wind speed during the day (see Fig. 4.1b). The low wind speed during the night might result from a decoupling by the stable boundary layer.
In contrast to the observation the model runs show an underestimation of both the anabatic and the katabatic wind. During the day the underestimation is larger as coarser the model resolution gets. Additionally, SU7 shifts the peak of the anabatic wind towards earlier times. The peak of the anabatic wind is well represented in the other two model runs (SU1 and SU2).
During the night the situation is somehow different. The coarsest model run (SU7) shows the best fit to the observation, whereas SU2 not even simulates a katabatic wind during night.
The onset of the anabatic forcing period is different regarding the simulations and the observation. The onset is around 2 hours earlier in the two finer model runs than the observation which occurs around 0900 UTC.

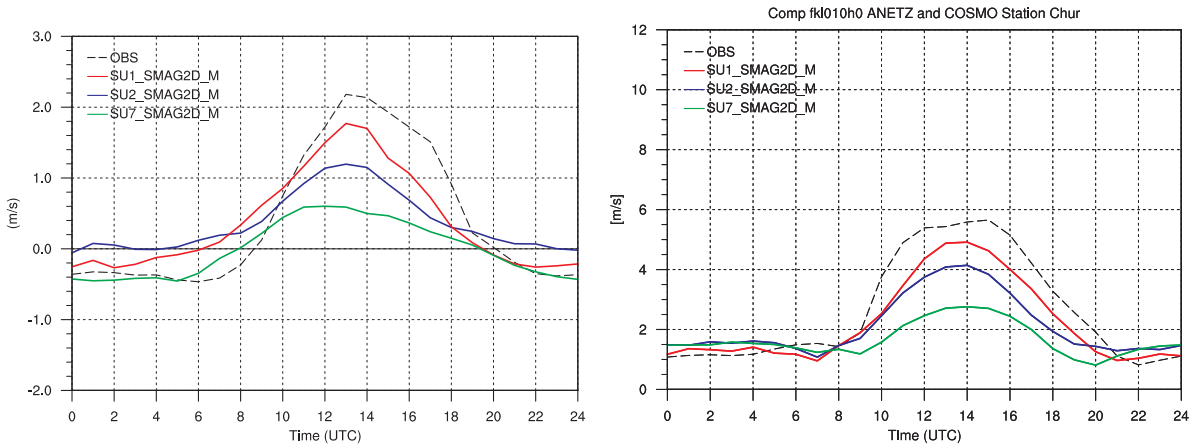

(a) (b)

Figure 4.1.: (a) Mean diurnal cycle of anabatic valley wind. The wind speed (m s^{-1}) is computed as average over six valleys and July 2006 from the (black) observations and simulations (SU1 (red), SU2 (blue) and SU7 (green). (b) Mean diurnal cycle of wind speed (m s^{-1}) at the valley station Chur from observations (black), SU1 (red), SU2 (blue) and SU7 (green).

4.2. Radiation

An important factor for the evolution of the valley wind system plays the available energy which determines the heating. To see whether the model can capture well the incoming and outgoing radiative fluxes at the surface a comparison between the model runs and the ASRB dataset was done (see section 3.2). Unfortunately, the radiation budget was not available at the six selected valleys but the ASRB dataset reflects characteristics of stations located in the Alpine region.

In Fig. 4.2a the net radiation (NR) in the ASRB station Davos is represented. NR is calculated as

$$NR = SWin + SWout + LWin + LWout. \tag{4.1}$$

The station Davos is chosen, because of its good representation of a station located in the Alpine region. The radiation budget for the other two fully equipped ASRB stations (Versuchsfeld SLF and Cimetta) are added in the Appendix E. For all three stations the findings are similar.
All three model runs are generally capable to capture the NR. The difference between the three model runs is small. All runs show an underestimation of NR. The onset and decay of NR is earlier and later, respectively which could possible come from missing topographic shading in the model. Decomposing the radiation budget in its components (see Fig. 4.2b) reveals that the more narrow NR curve results mainly from SWin. SWin is underestimated more strongly with coarser horizontal resolution. Thus, all three runs underestimate SWout, which is linked to the surface albedo. Hence the net shortwave radiation will be underestimated too.

SU2 shows the smallest underestimation of LWout. LWout is coupled to the surface temperature by the Stefan-Boltzman-Law, which means that the error of LWout could stem from the modelled surface temperature. Unfortunately, no observed surface temperatures were available, but an underestimation could be possible, since the 2m-temperature perturbations are also unterestimated during the day (see Fig. 4.4a).
It appears to be difficult to simulate LWin, since the downward radiation is highly influenced by the emission from clouds. At the station Davos LWin is well represented in all three runs. However, regarding the other stations (see Fig. E.1 in the Appendix) SU7 overestimates LWin especially at station

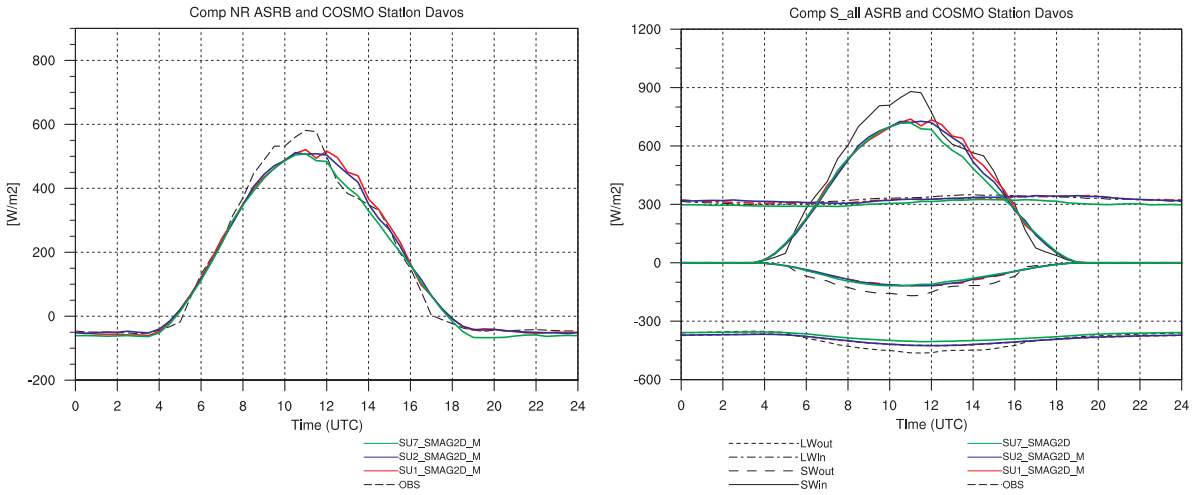

(a) (b)

Figure 4.2.: Diurnal cycle of surface radiation budget at ASRB station Davos for the whole July 2006: (a) net radiation (W m^{-2}); (b) individual parameters of radiation balance. SU1 in red, SU2 in blue, SU7 in green and observation in black.

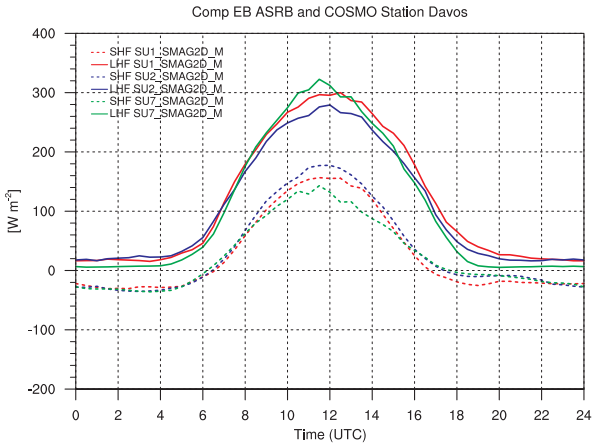

Figure 4.3.: Partitioning of the available energy in sensible (SHF) and latent (LHF) heat flux (W m^{-2}) for ASRB station Davos for the whole July 2006. SU1 in red, SU2 in blue and SU7 in green. No observations are available.

Versuchsfeld SLF whereas all runs overestimates LWin at station Cimetta. This overestimation during the night reflects the effect of too high cloudiness during nighttime period in the coarser model runs (see section 4.6).

To complete this analysis of the surface energy budget, sensible (SHF) and latent (LHF) heat fluxes are investigated. Surface heat fluxes are not available from the here used observational datasets, but are calculated in the model (see Fig. 4.3). The partitioning of LHF and SHF is different between the finer model runs and the coarser model run. SU7 shows considerably more LHF than SHF wheras SU2 represents less LHF and more SHF compared to the others. It is still an open question why the two finer model runs differ as well so much in partitioning of LHF and SHF. The relation could not be seen from potential temperatures (see section 4.3). For a different partitioning surface properties might be different. The SU1 surface properties were calculated using a nearest neighbour interpolation from the SU2 surface properties, thus surface properties should be identical between these runs. However, the topography differs between these runs and has an impact on the elevation of the grid-point in the simulations.
A wrong partitioning of the surface heat fluxes could be an answer of the in general too cold simulated temperatures (see Fig. 4.4a), meaning that in all model runs LHF is overestimated.

4.3. Potential temperature perturbations

Because of the different valley-volume between a valley and a plain a temperature difference between the air in the valley and the air over the adjacent plain evolves. The temperature amplitude within the valley should be greater than the amplitude over the adjacent plain. The valley atmosphere should be warmer during day (with respect to the plain) and colder during night. This temperature difference drives the pressure gradient and hence Alpine pumping (Whiteman, 1990). The underestimated SWin in the model runs as discussed above, will have implications in the available energy for heating the valley-volume.

Unfortunately, only surface measurements of temperature are available and thus the whole air column could not be investigated within the selected valleys.
Figure 4.4a shows the mean diurnal cycle of potential temperature perturbations averaged for the six valley stations (solid) and their six plain counterparts (dashed) for July 2006. The three model runs (SU1 in red, SU2 in blue and SU7 in green) were compared to the observations (in black). A perturbation is a departure from a 'mean' state. For the calculation the 'mean' value of potential temperature as a 24-hours mean is substracted to remove the diurnal temperature variations.
The maximum of observed potential temperature perturbation in the valley is achieved around 1300 UTC whereas the plain maximum occurs later around 1500 UTC.
The modelled potential temperature perturbations are generally not as large as the observed ones and achieved earlier. The two finer resolutions (SU1 and SU2) show only small differences whereas the coarser resolution (SU7) shows both a smaller amplitude and an earlier heating and cooling. SU7 shows further an enhanced heating in the valley stations in the morning hours around 0800 UTC. Overall the potential temperature perturbations are mainly underestimated during the day and during the night in all model runs. The daytime underestimation might be linked to an underestimation of SWin during the day (see Fig. 4.2), the nighttime overestimation to an underestimation of LWin due to overestimated high cloud cover during night (see section 4.6).

Concerning the observations the evolution of Alpine pumping is visible from 2-m potential temperature perturbations. The heating of the valley atmosphere is larger during day and smaller during night. The changes occur around 0800 UTC and 1900 UTC. In contrast all three simulations show stronger warming for the plain stations during day and stronger cooling during night.

All three model runs are also shifted in time with respect to the observations and are therefore in phase with the earlier onset in mean anabatic wind (see Fig. 4.1). This means that the sign-change of pressure difference should occur earlier compared to the observations.
The along-valley wind systems occur as a result of a greater diurnal temperature in the air column within the valley than in the plain. This differential heating produces a pressure gradient (see section 4.4) which itself causes the valley wind system (Whiteman, 1990). Since only surface measurments of temperature are available a direct link from the calculated potential temperature perturbations and the pressure gradient is problematic.

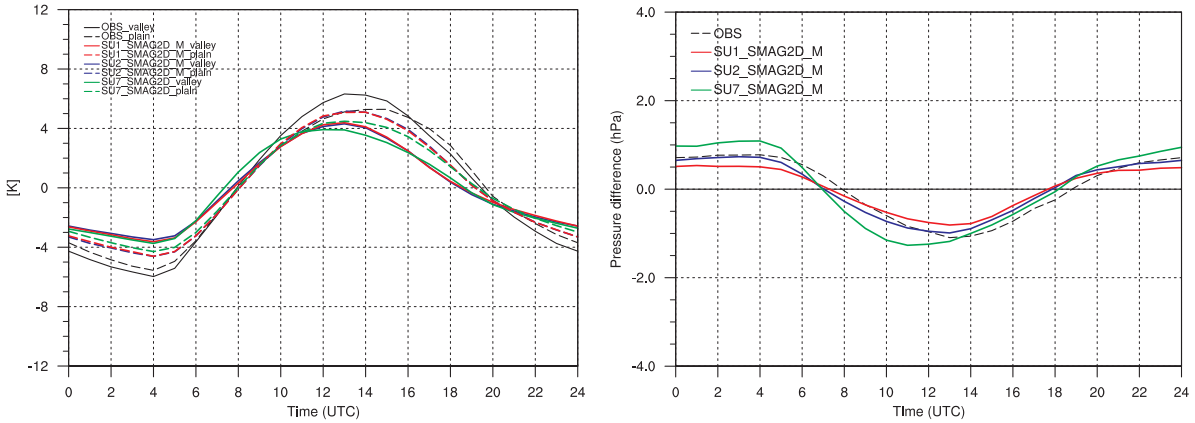

(a) (b)

Figure 4.4.: Observations (black), model run SU1 (red), model run SU2 (blue) and model run SU7 (green). (a) Mean potential temperature perturbations (K) using six selected valley stations (Chur, Sion, Altdorf, Interlaken, Innsbruck and Garmisch; solid) and their counterpart plain stations (St.Gallen, Bern-Liebefeld, Wynau, Basel, Munich; dashed). (b) Mean diurnal horizontal pressure difference (hPa) calculated using the six selected valley stations and their plain-counterparts.

4.4. Pressure difference

In Fig. 4.4b the mean horizontal pressure difference is calculated with the selected six valleys as described in section 2.1. This method for calculating the pressure difference works well even for short time series. A calculation of a pressure gradient as in Lugauer and Winkler (2005) gives not nearly the same result as with the calculation as in Geerts et al. (2008). The calculation of Lugauer and Winkler (2005) is strongly dependent on long time series (climatologies).

The calculated mean horizontal pressure difference reflects well the theory. During the night the pressure difference (calculated as valley-plain) is positive (lower pressure over the plain than in the valley), whereas during the day the pressure difference is negative (higher pressure over the plain than in the valley). The result of this changing pressure difference is a plain-to-mountain circulation pointing towards the mountain during the day and away during the night (see Fig. 4.1a). The driving force behind this changing pressure difference is the different heating in valleys and their corresponding plains (Whiteman, 1990)g.

Overall, the models can capture the diurnal variations very well. A noticeable shift in the timing is visible in all three model runs and is especially distinct as coarser the horizontal resolution gets.
SU7 shows an overestimation of the pressure difference during night and during day. Further, the maximum of the pressure difference is reached around 2 hours before the observations. The enhanced pressure difference in the morning hours is in accordance with the enhanced heating in the valley stations

around the same time (see section 4.3).
On contrary, the difference between the two other model runs (SU1 and SU2) is small, however, both runs show an underestimation during night and during day, most pronounced in the highest model resolution. This is in agreement with the discussed problem of a smaller potential temperature perturbation amplitude in the model, which provides too small forcing for the build-up of a pressure gradient. But, the potential temperature perturbations are only surface measurements and therefore not valid for the whole air column in the valleys. The underestimation of the pressure difference is linked to the larger potential temperature amplitude at plain stations compared to the valley stations in the model (see Fig. 4.4a). This impact of potential temperature amplitude on pressure difference can not be explained regarding SU7. Even though potential temperature perturbations are underestimated in SU7 as well, pressure difference is overestimated during day and night. The enhanced heating in the morning hours could lead to the overestimated pressure difference during the day. However, the overestimated pressure difference during night is not in agreement with the potential temperature perturbations. Further, even though the pressure difference is overestimated in SU7 this larger drive is not visible in the anabatic wind (see Fig. 4.1).
All runs show also an earlier change to the negative pressure difference in the morning hours and an earlier change to a positive pressure difference in the afternoon hours. This earlier sign-change is in agreement with the earlier onset of SWin possibly influenced by the neglect of topographic shading. Overall the two finer model runs capture well the amplitude of the pressure difference compared to the observations, but show difficulties in the transition hours.

4.5. Precipitation

To quantify the link between Alpine pumping and convective precipitation, mean diurnal cycle of precipitation (observed as well as modelled) has been analysed. Since the gridded observational data is available only over Switzerland the modelled precipitation has also been averaged over Switzerland. Modelled precipitation has been interpolated to the grid of the observational dataset. Figure 4.5 shows both simulated and observed precipitation over Switzerland. Both analysis period are showed because they differ in some points.

As shown in the literature (see e.g. Germann et al., 2006) the estimated rain amounts from radar measurements can be strongly biased. However, rain-gauge measurements usually underestimate the total convective precipitation amount (Frei and Schär, 1998). Therefore this two observational data sets can be viewed as upper (RAD) and lower (DES_GAUGE) limit of rain rates.

Obviously, the difference between SU1 and SU2 is small. Both runs produce more precipitation than DES_GAUGE and less than RAD and are therefore capable of simulating the peak amounts. The onset of precipitation is also well represented. One particular deficit of the convection-permitting simulation appears to be the overestimation during nighttime and the late evening. During the weak synoptic period a slight second maximum of precipitation during the night is visible. Comparing the two analysis periods further, shows a reduction of precipitation especially in the model runs SU1 and SU2. During the period with weak synoptic forcing the simulated rain amount is closer to DES_GAUGE than to RAD. Further, the nighttime precipitation amount is reduced, but nevertheless significantly overestimated.
SU7 shows an earlier initiation of convection for both analysis periods (around 2 hours). Regarding the whole month the amount of precipitation in SU7 is reduced compared to the other model runs. Further SU7 shows a pronounced second maximum of precipitation especially during the early morning of the synoptically weak period.

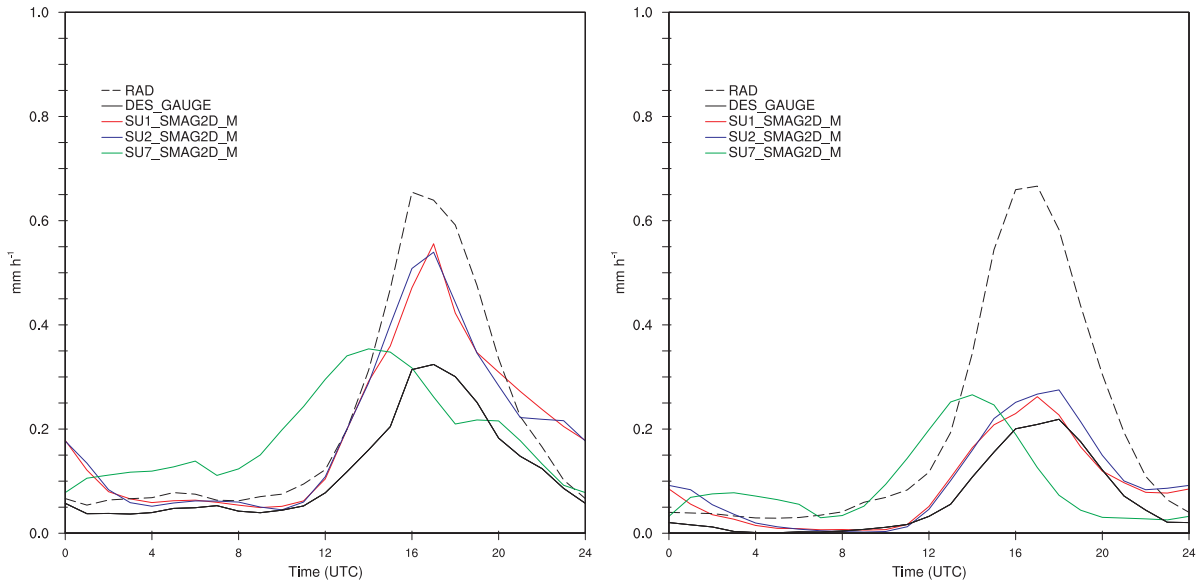

Figure 4.5.: Mean diurnal cycle of precipitation (mm h^{-1}) averaged over Switzerland for period (a) from 0600 UTC 01 July 2006 until 0600 UTC 31 July 2006 and (b) from 0000 UTC 09 July 2006 until 0000 UTC 27 July 2006. Observations are indicated by black lines, SU1 in red, SU2 in blue and SU7 in green.

4.6. Satellite data

Until now, with exception of the radar measurements, surface observations have been validated. To gain further insight into the interaction between the valley-wind structure over the Alpine region a validation using satellite data was helpful. As described in section 3.3.3, COSMO is able to generate synthetic satellite images. These images were compared to the satellite images obtained from Meteosat 8 (see section 3.2).
A comparison between the observed BT and modelled BT at 10.8 μm was performed to enhance the understanding of the representation of cloud amount and cloud patterns in the model.

Figure 4.6 shows a situation typically observed during midday. BT from three model runs and the satellite are shown in Fig. 4.6 for 1230 UTC 13 July 2006.
The observation shows the initiation of deep convection over the Black forest, Vosges, the Jura chain and localized regions in the Alps. SU1 and SU2 show a slightly delayed initiation, but a good agreement in its location. The large cloud structure over the Austrian and Italian Alps is a remainder of the previous day's convective cloud cover, which is also visible during nighttime. However, SU7 deviates considerably from SU1 and SU2. SU7 shows pronounced convective clouds over most parts of the domain. This is in agreement with the earlier onset of precipitation as seen in Fig. 4.5.
Figure 4.7 shows a mature stage of convective development for 1600 UTC 13 July 2006. SU1 and SU2 show pronounced convective regions over mountainous terrain, namely the Black forest, Vosges, Jura and the main Alpine chain. However, the observed cloudiness is pronounced over the Mittelland, southern Switzerland, and France, whereas in the model convection is restricted to the mountainous terrain. In contrast SU7 shows convection widely spreaded over the domain. Overall SU1 and SU2 reveal more small scale pattern compared to the observation.

As described in section 3.2.4 the difference between the 10.8 μm BT and the 6.7 μm BT can be used to detect overshooting convective tops. Fig. 4.8 shows the BT difference (BTD) 6.7 μm BT - 10.8 μm BT. A positive BTD can be related to deep convection. The runs (SU1, SU2 and SU7) and Meteosat on

1600 UTC 13 July 2006 are shown. This period was indicated above as mature stage of convection. It is visible that with this detection tool Meteosat 8 shows deep convection over the western part of Mittelland and South-Switzerland. These regions are in agreement with the cold BT detected in the infrared channel in Fig. 4.7d. SU7 shows deep convection spreaded all over the domain, whereas SU1 and SU2 represent only few deep convection pattern. SU1 reacts, compared to SU2, slightly faster, visible in more deep convection at 1600 UTC. Here, too, the restriction of deep convection in the convection-permitting simulations to the mountainous terrain is visible.

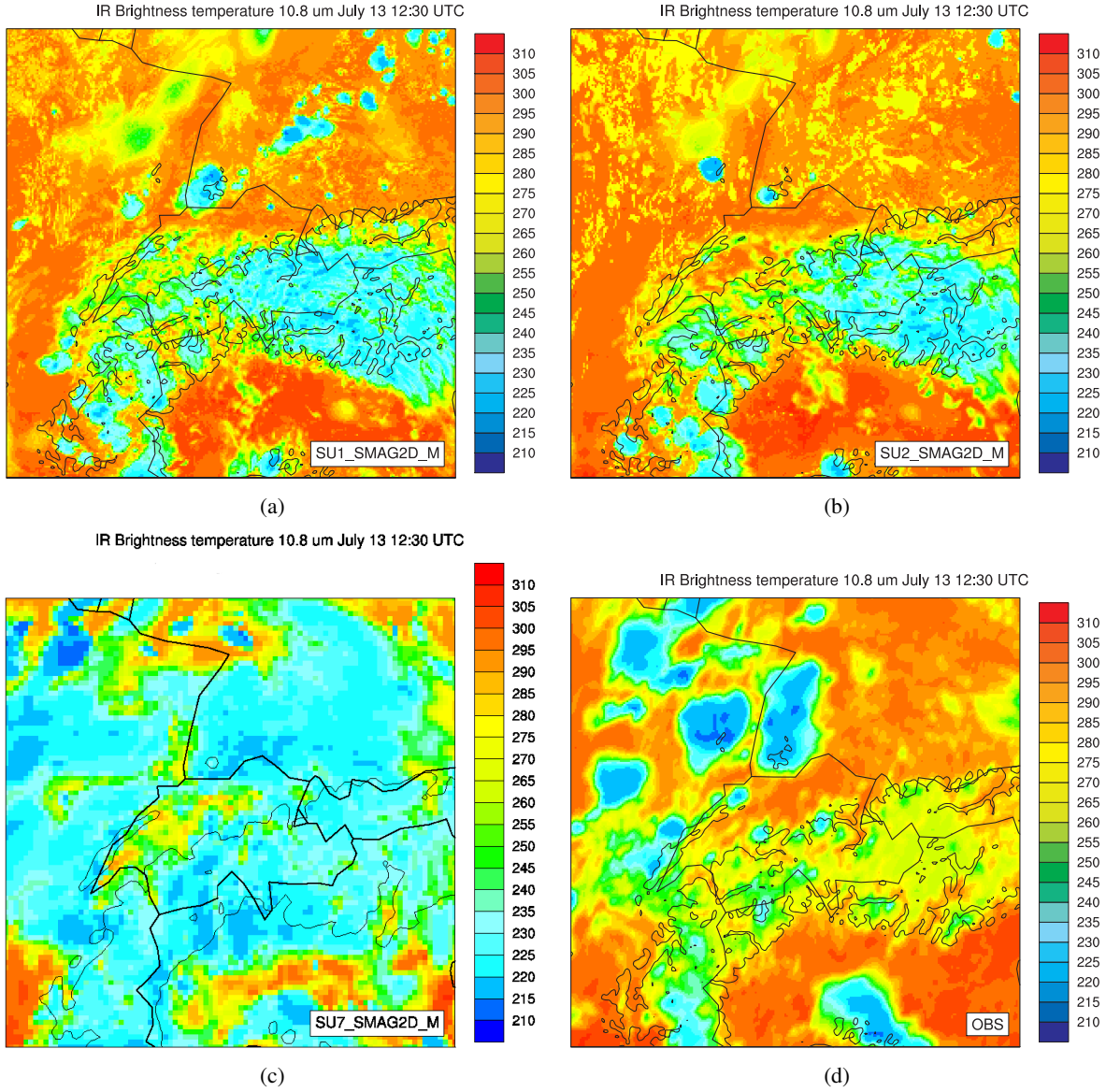

Figure 4.6.: Modelled and observed 10.8 μm BT (K) for a typical initiation of convection at 1230 UTC 13 July 2006. At this time simple convective cells are triggered over Vosges and Black forest mountains.

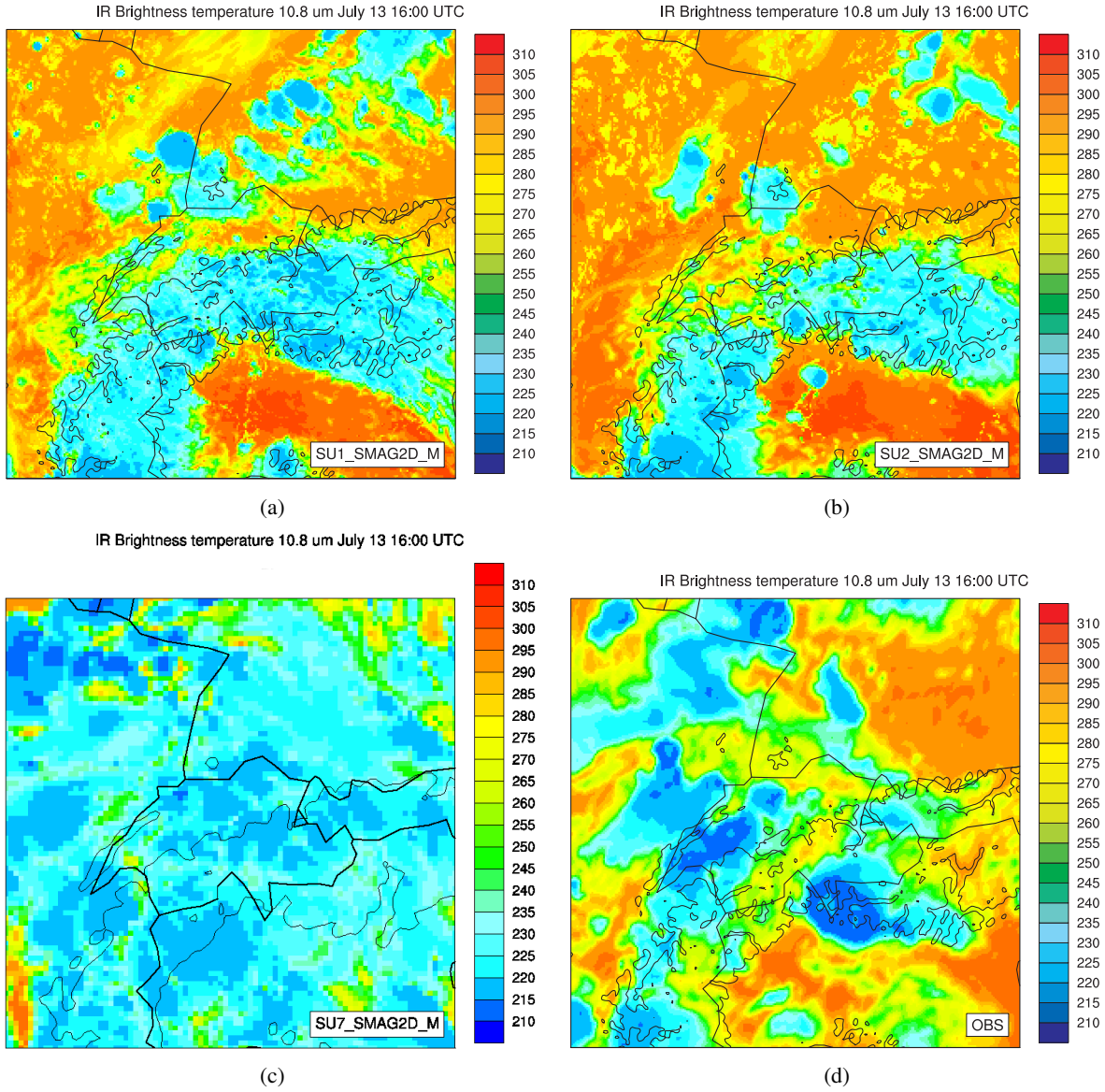

Figure 4.7.: Same as Fig. 4.6 but for a typical daytime situation at 1600 UTC 13 July 2006. At this time a mature stage of convection is reached.

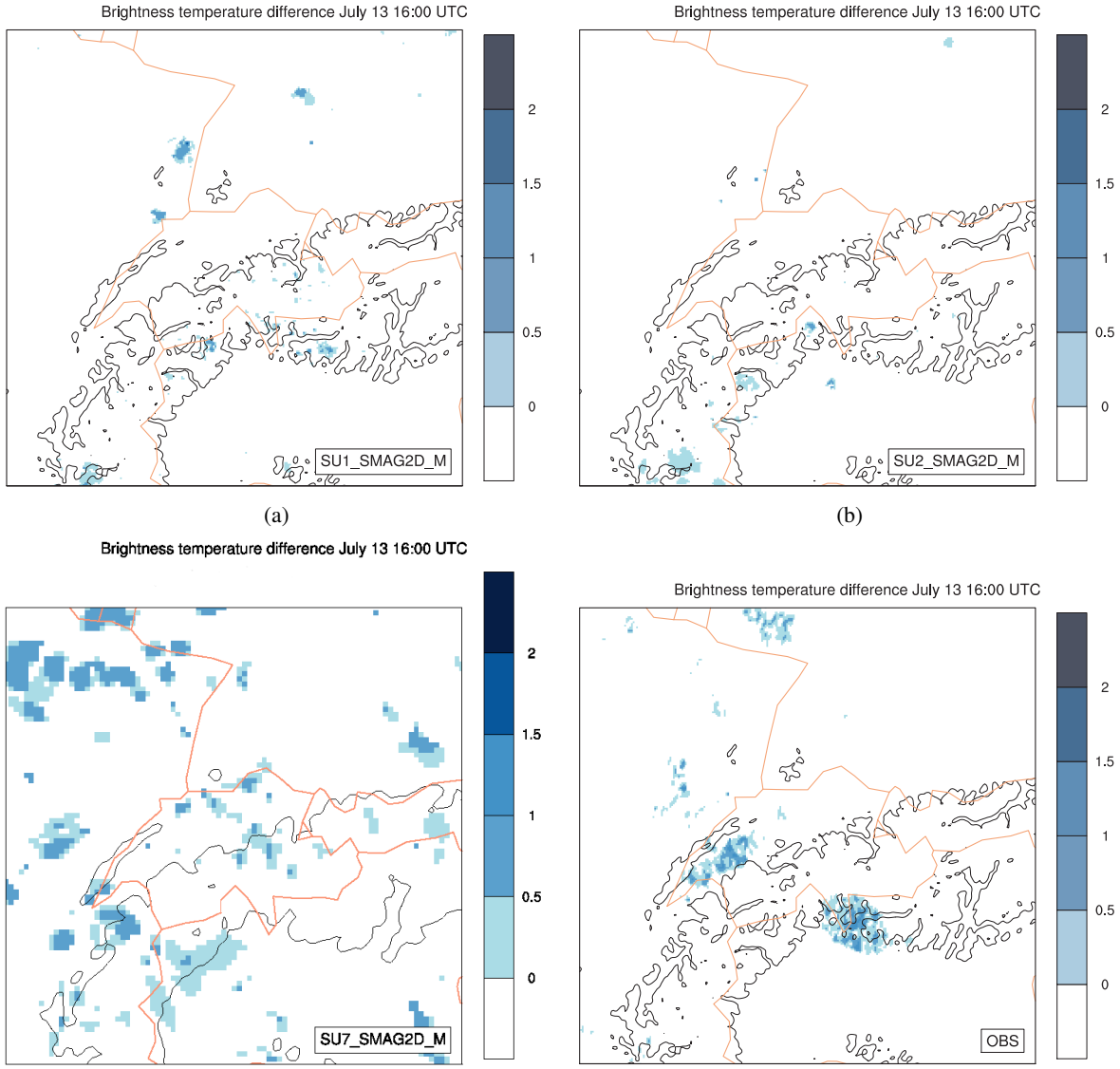

Figure 4.8.: Modelled and observed brightness temperature difference (K) at 1600 UTC 13 July 2006. At this time overshooting tops are visible in the observations during this mature convection stage.

5. Alpine-scale validation

As discussed in section 3.1.2 a larger Alpine region has been chosen to complete the study of the valley-wind system. The disadvantage is a limited availablity of observational data at this scale. Actually, only satellite data is available. The advantage is that the predictability is larger as larger the region gets. And with these results in the model simulations further insights are gained into the interaction of Alpine pumping with convective precipitation.

5.1. Precipitation

Previously, the precipitation amount was calculated over Switzerland to compare the simulations to the available observational data set. Here, rain rates have been averaged over this Alpine polygon (see Fig. 3.1) and are shown in Fig. 5.1. Additionally rain rates averaged over Switzerland have been drawn in Fig. 5.1.
Both SU1 and SU2 show a similar evolution with an initiation of precipitation around 1100 UTC and a peak around 1700 UTC. However, SU1 shows a slightly lower rain maximum during the weak-synoptic period. Again, SU7 shows an earlier onset of precipitation compared to the convection-permitting runs. SU7 also results in constant nighttime precipitation rate more than 0.1 mm h^{-1}.

A comparison between the rain amount over Switzerland with the rain amount over the Alpine polygon could be interesting. During daytime the rain rates are larger for the Alpine polygon during the weak synoptic period. However, considering the whole month the precipitation amount is similar over Switzerland and over the Alpine polygon (at least for SU1 and SU2). This suggests that the influence of the frontal systems is of particular importance for precipitation over the Mittelland and southern Switzerland. During the frontal passage moist air masses are advected towards Switzerland followed with partially heavy precipitation (around 37 mm daily sum for station Lugano and 06 July 2006) (MeteoSchweiz, 2006). Compared to the precipitation in Switzerland, SU7 decreases the rain amount during the whole month. Hence, see Fig. 5.1a, SU7 underestimates the rain amount especially over the Mittelland. This was also shown by Hohenegger et al. (2008), who's coarse-grid run also underestimates the rain amount over flat regions in Switzerland.
During the night the rain amount and the secondary peak is increased compared to the precipitation in Switzerland. This shows that the precipitation during night is mainly initiated over the mountains rather than over the plain.
Comparing further Switzerland versus Alpine polygon shows that the peak is reached at the same time in the Alpine polygon and in Switzerland. This could also be seen when regarding the satellite images. The initiation of convection happens around mountainous terrain (see Fig. 4.6) and stays there for the model runs. Probably for the observations the peak of rain rates in the Alpine polygon would be shifted towards earlier hours than the peak over Switzerland. During the day convection is translocated towards the Mitteland or southern Switzerland thus over flat regions in the observations. This translocation of convection may appear in the precipitation peak which probably occurs later including the plain than only over the mountain in the observations.

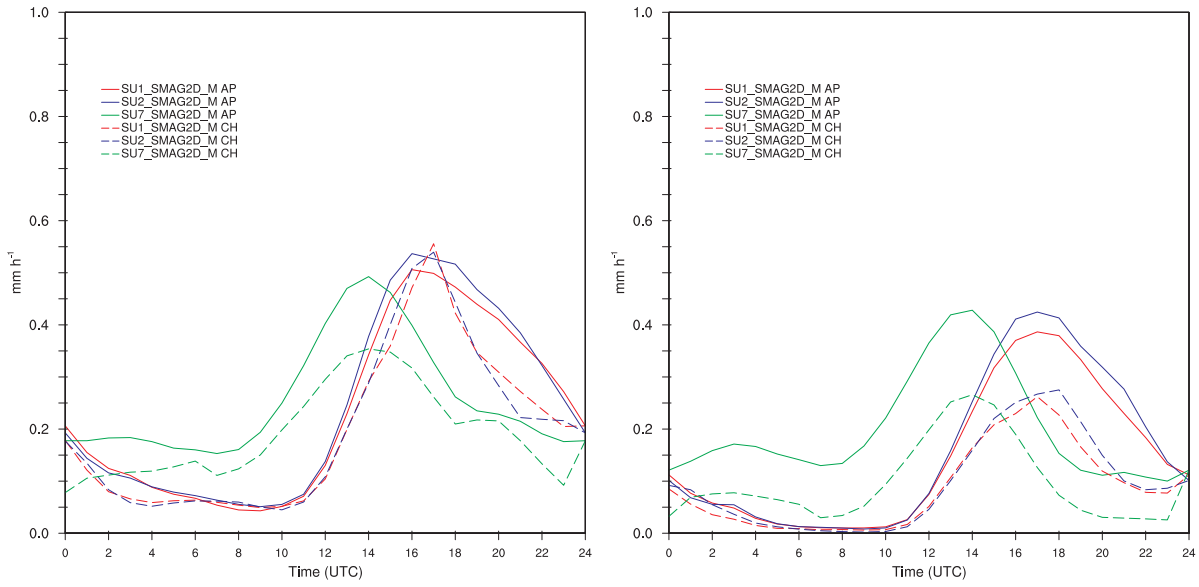

Figure 5.1.: Mean diurnal cycle of precipitation (mm h^{-1}) averaged over Alpine arc (solid curves) indicated in Fig. 3.1 and averaged over Switzerland (dashed curves) for period (a) from 0600 UTC 01 July 2006 until 0600 UTC 31 July 2006 and (b) from 0000 UTC 09 July 2006 until 0000 UTC 27 July 2006. Observations are indicated by black lines, SU1 in red, SU2 in blue and SU7 in green.

5.2. Satellite data

As in Keil et al. (2006), histograms of observed and modelled BT were calculated over the Alpine polygon. Table 3.4 relates BT to specific heights and cloud types. The classification is the same as in Keil et al. (2006).

Figure 5.2 shows the relative frequency distribution of BT for the Meteosat 8 and the model runs. The relative frequencies are calculated over the Alpine polygon and averaged over the weak-synoptic period for one instant in time. Figure 5.2a shows the relative frequency distribution at 0400 UTC, a typical nighttime situation, Fig. 5.2b shows a typical situation for the beginning of convection at 1000 UTC and Fig. 5.2c shows the same at 1600 UTC for a typical mature stage of convection. During the night the model runs show considerably more high clouds than Meteosat 8 and less cloud-free or low-clouds (Fig. 5.2a). With the start of convection (Fig. 5.2b) Meteosat 8 shows growing in mid-level clouds around 1000 UTC visible in enhanced relative frequencies around 0°C. The simulations represent at the same time more high clouds which are a remainder of the cloud cover from the previous night. This remainding feature was also visible in Fig. 4.6a,b. The runs mainly underestimate the mid-level clouds, a feature that was also visible in spatial patterns of BT (see Fig. 4.6). .
However, in the mature convective stage (1600 UTC, Fig. 5.2c and also Fig. 4.7) the models overestimate high clouds, especially SU7, and underestimate mid-level clouds. This underestimation of mid-level clouds represents the difficulties to simulate adequately shallow convection. The overestimation of high clouds over the Alpine arc shows further, that the runs later translocate convection over the plain as could be seen in the observations (see Fig. 4.7d).

Figure 5.3 shows mean diurnal cycle of integrated frequency distribution. Following Keil et al. (2006), three categories are distinguished by integrating from -60°C to -20°C, from -20°C to 0°C, and from 0°C to 40°C, respectively. This differentiation allows to study the development of low clouds, mid-level clouds, and high clouds separately. Additionally, the precipitation rates in Switzerland and the Alpine

polygon are showed for each model run individually and for observations. The measurements are shown in Fig.5.3d. Mid-level clouds evolve around 0900 UTC and around 1100 UTC high clouds start to develop. This was also visible from Fig. 5.2b. Convection starts decaying around 1800 UTC until 0200 UTC and after that only mid-level clouds and cloud-free/low-clouds are visible.
A comparison of SU1 and SU2 with the observations reveals mainly two differences (Fig. 5.2a,b): Firstly, mid-level cloud fraction is smaller in the model runs. This reflects the fact that shallow convection is not simulated adequately. Secondly, high clouds decay too slowly in the model runs and persist over the night. The daytime peak in cloudiness is therefore simulated broader than observed. However the total fractional cloud cover of high and mid-level clouds is roughly the same in the observations and the convection-permitting models.
SU7 (Fig. 5.2c) shows even less mid-level clouds and a faster evolution of cloud pattern (around 1000 UTC). The high cloud amount stays always above 30 percent. In all simulations the start in convection occurs simultaneously in mid-level and high clouds. This fact is not visible in Meteosat 8 where a transition between mid-level clouds (shallow convection) and high clouds (deep convection) proceeds.

Regarding the rain rates, which are drawn as curves in each diagram, some interesting features are visible: With the onset of mid-level clouds precipitation is formed in the observations around 1200 UTC. The rain amount starts decaying while high-level clouds remain. The peak of the rain rate is reached at the same time as the peak in deep clouds (high clouds). In SU1 and SU2 the precipitation starts around the same time as in the observation. This is in phase with the evolution of high clouds in the convection-permitting models. SU7 shows also an in phase evolution of high clouds and precipitation but shifted earlier in time regarding the observations and SU1 and SU2, respectively.
However, overall the cloud pattern evolution is in accordance with the overall evolution of precipitation. SU7 shows a faster evolution of high cloud pattern (convection) and a earlier precipitation peak. The two other runs show a later precipitation peak resulting from the later cloud/convection evolution.

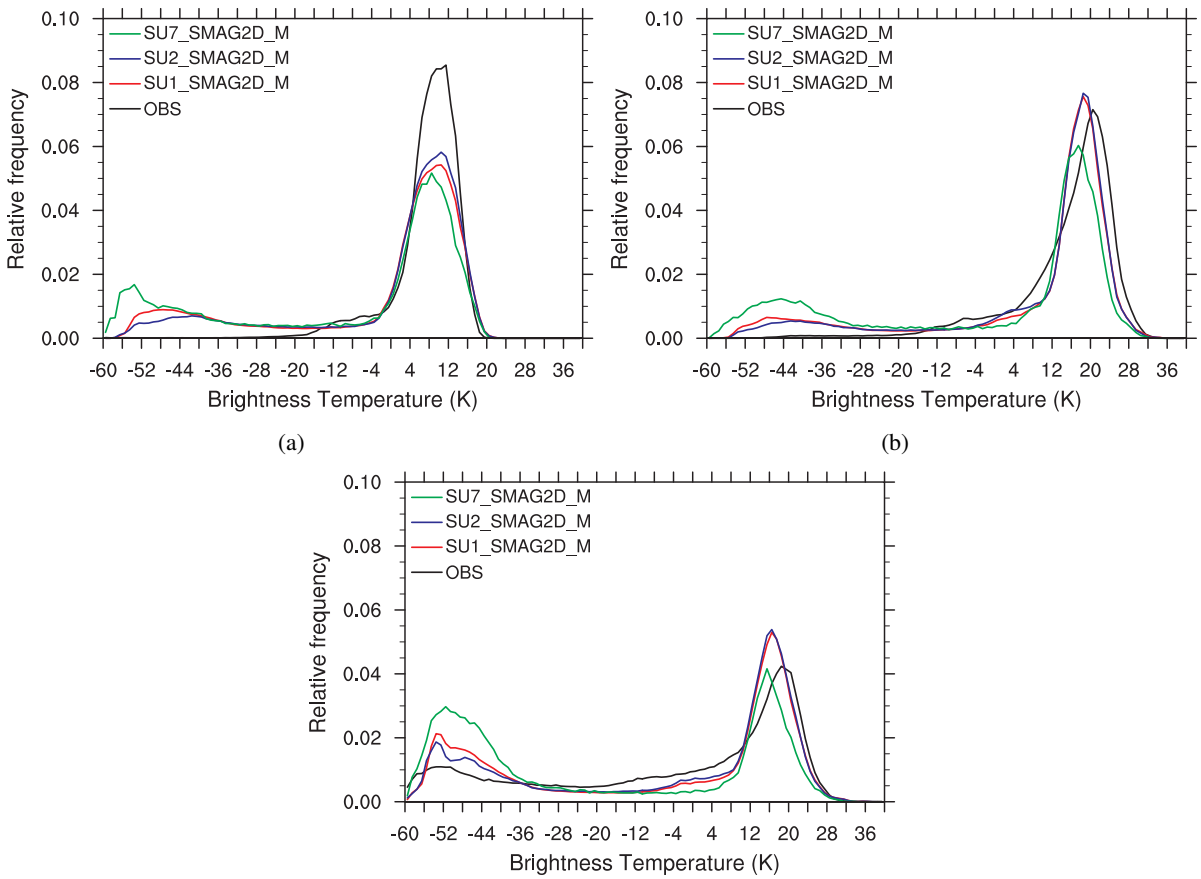

Figure 5.2.: Averaged histograms of BT (K) for the weak-synoptic period of the models (SU1 in red, SU2 in blue and SU7 in green) and Meteosat (in black) in the IR channel at (a) 0400 UTC, (b) 1000 UTC and (c) 1600 UTC.

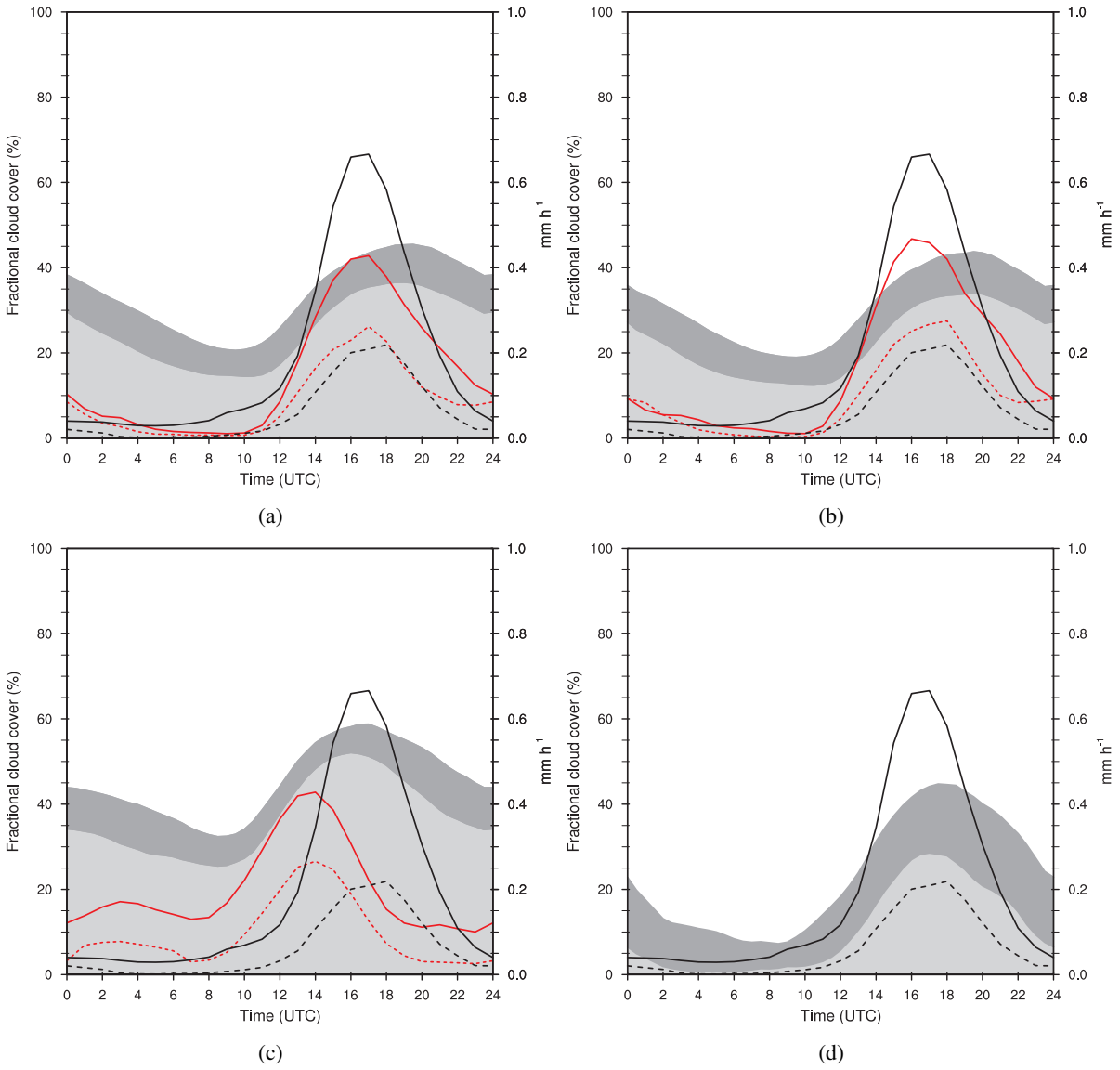

Figure 5.3.: Mean diurnal cycles of integrated BTs for the weak synoptic period for (a) SU1, (b) SU2, (c) SU7 and (d) Meteosat 8. Three categories have been distinguished: high clouds (light grey), mid-level clouds (dark grey) and low clouds/cloudiness regions (white). Additionally mean precipitation rates (mm h^{-1}) for each model run are drawn individually (red, solid: for model runs rain amount over Switzerland; red, dashed: for model runs rain amount over Alpine polygon; black, solid: DES_GAUGE precipitation amount over Switzerland; black, dashed: RAD precipitation amount over Switzerland).

5.3. Mass convergence

As described in section 2.2 the mass convergence is calculated for the Alpine polygon. The results of the model runs could be useful to relate the mass convergence to the triggering of convection. In Fig. 5.4 the mass convergence is plotted for each model run and the two analysis periods.
The differences between the two analysis periods are small. This suggest that during the synoptically-forced period mass convergence is very similar to the weak-convective period (Fig. 5.4b).
Regarding first only SU1 and SU2: SU1 and SU2 show the same evolution of mass convergence with the onset around 0700 UTC, a peak around 1300 UTC, and a return to divergence at 1730 UTC. The difference between the two is larger during night where SU1 shows less divergence than SU2. The onset of convergence and the return to divergence is around the same time as anabatic wind (Fig. 4.1a) and pressure difference (Fig. 4.4b) in the valley-scale validation. Before the peak of mass convergence occurs deep convection evolves in the model runs around 1100 UTC (Fig. 5.3a,b). The peak of mass convergence is then in phase with anabatic wind and 4 hours later, shortly before the change to divergence, the peak of rain rates is achieved (around 1700 UTC). With these relationsships mass convergence could sustain or facilitate deep convection seen in convection-permitting models. Further, deep convection may suppress mass convergence.
SU7 shows a lower and earlier peak of the mass convergence. This is in agreement with the lower and earlier peak of anabatic wind. The earlier onset of mass convergence could be seen in an earlier onset of pressure difference (Fig. 4.4b) probably due to enhanced heating in the morning hours in the valley stations (Fig. 4.4a). Deep convection is evolving shortly after the onset of mass convergence (Fig. 5.3c). However, the smaller peak of mass convergence is not in agreement with the larger simulated pressure gradient during the day. Furthermore, the peak of mass convergence happens roughly at the same time as the peak of precipitation rates. Convergence is maintained until 1900 UTC in the evening leading to a broader curve of mass convergence. This feature could not be observed in anabatic wind or pressure gradient where the sign-change occured at the same time as SU1 and SU2. In fact, SU7 shows an earlier precipitation peak but not an earlier mass convergence peak. This assumes the subordinate role of mass convergence on convective precipitation at least with a convection-parameterization scheme.

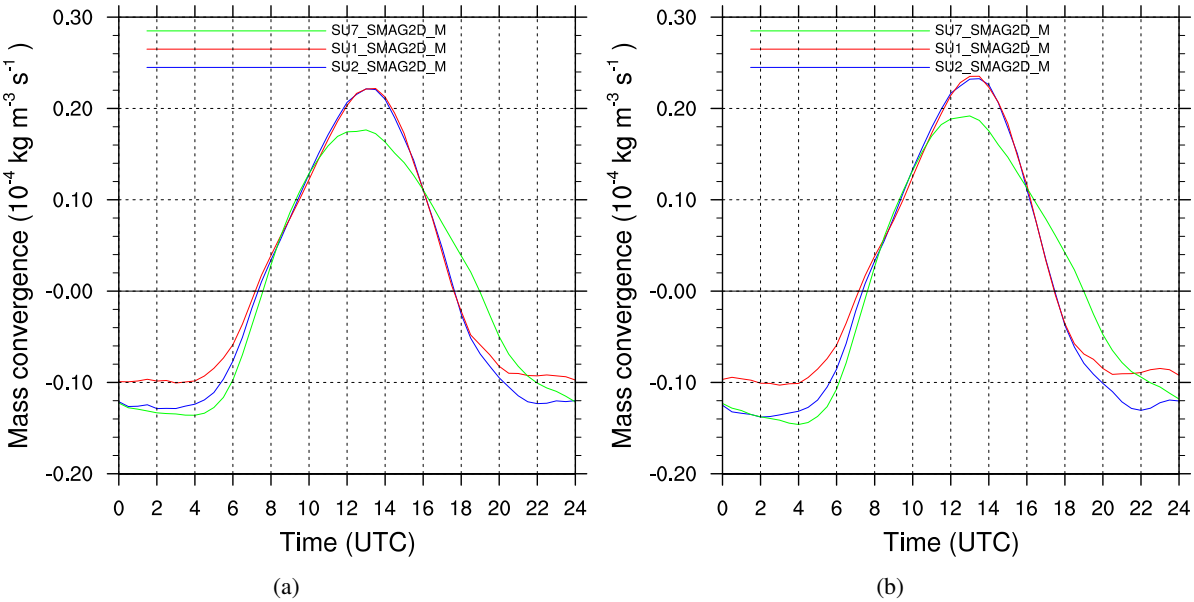

Figure 5.4.: Mass convergence (kg m^{-3} s^{-1}) for (a) the whole July 2006 (01.07.2006 07 UTC until 31.07.2006 18 UTC) and (b) for the middle of July 2006 (09.07.2006 00 UTC until 27.07.2006 00 UTC). Red: SU1, blue: SU2 and green: SU7.

6. Modelling sensitivities

Aiming at an improved agreement between forecasts and observations, modelling sensitivities have been studied in this thesis. Table 3.3 shows all conducted model runs. Additional experiments have been conducted with lexpcor=.False. (_LEXPCOR runs) and an improved aerosol climatology (_AER runs). The effect of these two modifications on Alpine pumping and its interaction with convective precipitation is described here.

In COSMO the tendencies from turbulent transport are computed in the planetary boundary layer parameterization for conserved variables. Thus, explicit corrections of these tendencies had been implemented originally to compute the tendencies for the non-conserved prognostic variables. Unfortunately, this correction (lexpcor=.True.) was not solved correctly, such that numerical errors affected both the heat and moisture budget. The results seems to be better with lexpcor=.False. and therefore two new model runs are conducted with lexpcor=.False.
For climate-scale Zubler et al. (2011) investigated the impact of a new aerosol climatology compared to the old aerosol climatology after Tanré et al. (1984). With the old aerosol climatology (Tanré et al., 1984) the aerosol optical depth is overestimated over the European continent leading to a smaller surface solar net radiation. With the new aerosol climatology the surface solar net radiation is increased by 20 W m^{-1} in the Mediterranean region (Zubler et al., 2011). Already Hohenegger and Vidale (2005) showed that COSMO uses a too large aerosol load over Europe and hence underestimates incoming solar radiation at the surface. Therefore runs were conducted using the aerosol climatology after Tegen et al. (1997).

As described in section 4.2, the model runs are capable to simulate the radiation and surface energy balance but underestimate especially SWin. As SWin is a crucial parameter for the available energy to drive Alpine pumping a correct simulation of SWin is of interest in this study.

The influence of the new aerosol climatology is strongly visible in the radiation balance which was also expected after the studies on aerosols in COSMO (Hohenegger and Vidale, 2005, Zubler et al., 2011). Figure 6.1a shows the NR for the two model runs for the ASRB station Davos. NR is up to 100 W m^{-2} increased improving the overall evolution of NR with respect to the observation. This effect is directly visible in the radiation balance (see Fig. 6.1b). SWin is also up to 100 W m^{-2} increased at the station Davos. This is in accordance with Zubler et al. (2011) who found in summer a maximum increase in SWin of roughly 85 W m^{-2}. This enhanced SWin and therefore the larger energy which is available is expected to enhance potential temperature perturbations and the pressure gradient.
The influence of the new aerosol climatology on the other radiation parameters is small. Only an improved SWout is achieved which could mainly come from a better overall representation of NR and hence a better partitioning between the individual parameters of the radiation balance.
In Appendix E the figures for the other two ASRB stations are added. The findings are similar to the station Davos, however Versuchsfeld SLF shows an too large increase of SWin with the new aerosol climatology compared to the observations. Since SWin is influenced by cloud cover and the difference between Davos and Versuchsfeld SLF is large, this feature is probably due to localized cloud cover above the station Versuchsfeld SLF.

This enhanced SWin should have an influence on other parameters. The figures from the pressure difference and the potential temperature perturbations with the new model run SU2_AER are added in

the Appendix chapter F and G. Model comparison with SU1 and SU1_AER were also done and showed similar results but are not included in this thesis.
The difference between the simulated pressure difference using the old aerosol climatology (Tanré et al., 1984) and the new aerosol climatology (Tegen et al., 1997) in finer model runs is marginal but the new runs (_AER) show a slightly increased pressure difference (see Fig. F in Appendix). The maximum is slightly shifted towards earlier hours but not consistently at all stations. This is in accordance with the changes in potential temperature perturbations. The 'new' model runs (_AER) show slightly warmer potential temperature perturbations during day and slightly cooler during night hence a larger overall temperature amplitude (see Fig. G in Appendix). This larger temperature amplitude results therefore in a slightly increased pressure difference. In total the differences between pressure difference and temperature variations and the two different model runs are small suggesting a small model setup sensitivity to these parameters.

The effect of the radiation balance should also directly have an effect on the precipitation amount. In Fig. 6.2 on one hand the mean precipitation amount averaged over Switzerland for the two analysis periods is shown (Fig. 6.2a,b). On the other hand the different model runs are drawn averaged for the weak-synoptic period and over Switzerland (Fig. 6.2c,d).
During the night the new model runs show a less pronounced second maximum of precipitation mostly visible in the weak-synoptic period. The reduction of nighttime precipitation is faster in the new model runs. The influence of the modifications on the daytime precipitation amount is strong. Eventhough the rain amount is similar between the model runs, both new runs show an earlier onset of precipitation. Figure 6.2c,d shows that the earlier onset is partly due to lexpcor=.False., and partly due to the new aerosol climatology. The earlier onset leads also to an earlier peak of precipitation rate in the new model runs. A possible explanation of this phenomenon could be the changed radiation balance and the slightly stronger pressure gradient and potential temperature perturbations.

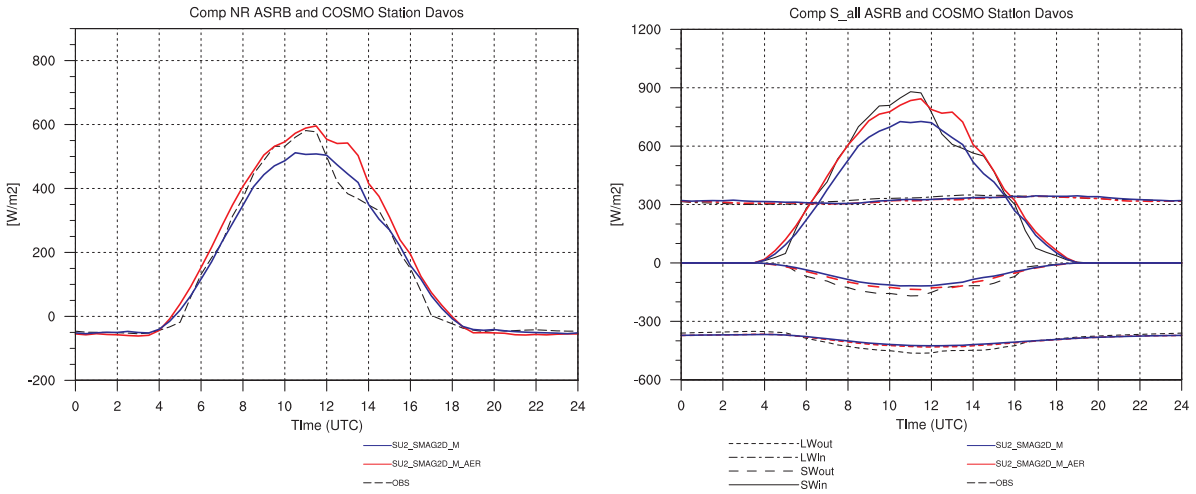

(a) (b)

Figure 6.1.: Radiation balance ((a) net radiation (W m^{-2} and (b) individual parameters of radiation balance) for ASRB station Davos for the whole July 2006. SU2_AER in red, SU2 in blue and observation in black.

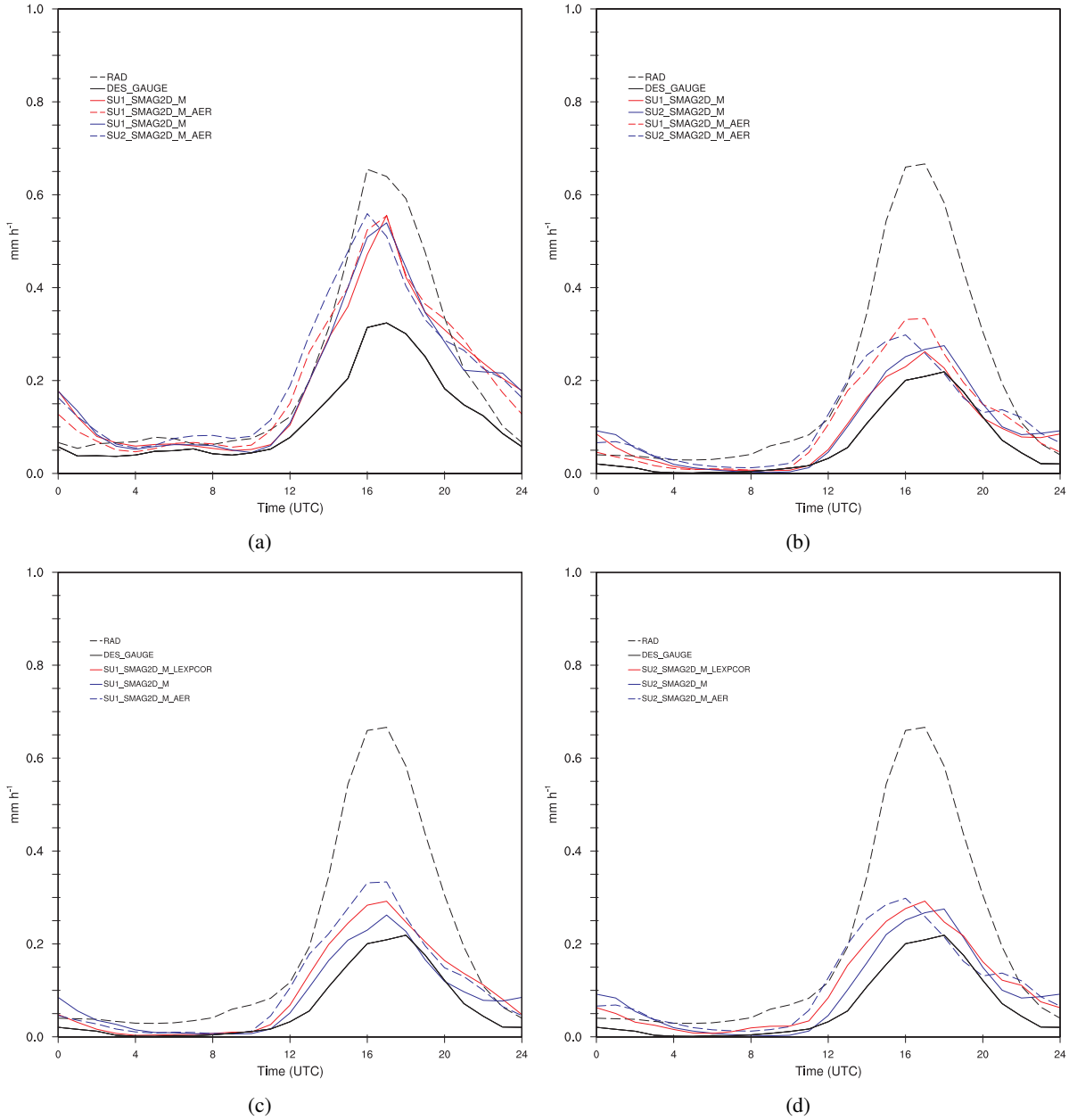

Figure 6.2.: Mean precipitation amount (mm h^{-1}) averaged over Switzerland (a) from 0600 UTC 01 July 2006 until 0600 UTC 31 July 2006, (b) from 0000 UTC 09 July 2006 until 0000 UTC 27 July 2006 for the new aerosol climatology. (c) shows the model runs SU1 and the different modifications in the weak-synoptic period, (d) represents the model runs SU2 and the different modifications also for the weak-synoptic period.

7. Discussion and Conclusion

Differential heating between Alpine valleys and the adjacent foreland induces a complex and multi-scale system of mass, heat, and momentum transport. In the Alpine region this thermally-induced circulation is called Alpine pumping and is observed frequently during flat-pressure distributions in summer. The interaction between thermally induced plain-to-mountain circulations and convection over mountainous terrain was subject in different studies (e.g. Demko et al., 2009, Demko and Geerts, 2010). Alpine pumping leads to a positive mass convergence over the Alps during the day. This horizontal mass flow will have an impact on the vertical mass flow due to mass conservation, which leads to an initiation or maintenance of convection over mountainous terrain. But different hypothesis have recently been suggested that the initation of deep orographic convection can not directly be related to this horizontal wind field and that deep convection may suppress mass convergence through cold-air outflow (Demko and Geerts, 2010).

The aim of this thesis was to quantify the observed and modelled thermally induced plain-to-mountain circulation, Alpine pumping, and to investigate the link with convective precipitation over the Alps. With reduced grid spacing in regional climate models a better representation of surface fields and topography can be realized. The better representation of the topography has a large impact in mountainous regions where a valley-volume is simulated more accurately. Additionally, deep convection can be explicitly resolved instead of parameterized.

For the purpose of this thesis mainly two numerical simulations with convection-permitting resolutions (CRMs) (O(1 km) and O(2 km)) and one simulation with coarser resolution (O(6 km)) with a parameterization scheme after Tiedtke (1989) were conducted and compared to observations. Simulations are performed for a period of one month, July 2006. July 2006 was characterized with a consistent flat pressure distribution (MeteoSchweiz, 2006), which is favourable for the evolution of Alpine pumping and a great likelihood for convective development. Two different validations were made regarding two scales in Alpine pumping: Firstly, valley-scale validations were performed looking at the scale of Alpine valleys and mainly on valley-wind systems. This validation consists of six pronounced valleys in the Alpine regions. Secondly, Alpine-scale validations were conducted looking at the scale of the whole Alpine arc and the overall plain-to-mountain circulation.

The main results concerning the simulations are as following:

- The incoming and outgoing radiation fluxes at the surface were simulated well in all three model runs. However, incoming solar radiation SWin and net radiation NR was slightly underestimated in all simulations. All runs showed further an overestimation of SWin in the morning and evening hours reflecting the neglected topographic shading effect.
- A comparison with surface station data in selected Alpine valleys revealed a very good agreement of horizontal pressure gradient and the daytime heating in the valleys. CRMs underestimated the daytime heating and the nighttime cooling in both, the valleys and the plains, respectively. Remarkable was a time shift towards earlier hours with coarser resolution. This underestimated heating and cooling in the valley atmosphere leaded to an underestimation of pressure difference during day and night in the CRMs. The time shift towards earlier hours was also visible in pressure difference. The peak of the pressure gradient occured slightly later than the maximum heating.

- The up-valley and down-valley wind was underestimated in all model runs. The initiation and decay of up-valley wind occured earlier in the runs compared to the observations. This is in agreement with an earlier sign-change in pressure gradient in the morning and evening hours. The same hold for the maximum of anabatic wind and the maximum of pressure gradient, which occured at the same time and therefore were shifted towards earlier hours with coarser resolution.

- The initiation of precipitation in the CRMs was in time with the observations and the daytime peak was in between the two observational datasets which can be regarded as upper (radar) and lower limit (gridded precipiation dataset) of the rain rate (Germann et al., 2006, Frei and Schär, 1998). But, the CRMs showed an overestimation of nighttime precipitation rate. The convection-parameterizing simulation showed the well known deficits of convection parameterizations: earlier initation of precipitation, earlier peak and distinct overestimation of nighttime precipitation rate.

- The simulation of three different cloud classes revealed interesting results. Meteosat 8 showed first, a development of mid-level clouds (shallow convection), and second, the evolution of high clouds (deep convection) which is in phase with the onset of precipitation. However, the evolution of mid-level clouds was underestimated in all three model runs such that the transition between shallow to deep convection did not occur in the model simulations. The high clouds persisted during the night in all runs.

The differences between the CRMs are overall marginal suggesting that below O(2 km) horizontal grid spacing the results of simulating Alpine pumping do not change substantial. However, the CRMs show a better representation of Alpine pumping and convective precipitation compared to the simulation with parameterized convection.
With the knowledge of these relationssships the interaction between Alpine pumping and convective precipitation could be studied:

- In the observations, the onset and maximum of precipitation occured around 3 hours after the onset and maximum of anabatic wind, respectively. However, the model runs showed an earlier onset of anabatic wind whereas the precipitation onset occured later in phase with the observations. The relationsship between inflow and evolution of convection was therefore visible in the observations but not in the model runs. This fact assumed that the relationsship between inflow and convection is not so strong. However, the runs underestimated the inflow which could not be strong enough to interact with the vertical flow.

- In all model runs the onset of the mass convergence was also around 3 hours earlier than the onset of precipiation. Hence after the onset of anabatic wind mass convergence can be observed. The peak of anabatic wind is in phase with the peak of mass convergence. The change to divergence in the evening hours occured roughly after the precipitation peak. Hence an interaction between mass convergence (Alpine pumping) and convective precipitation could still be possible.

These results could suggest that orographic convection is favoured due to the prevailing convergence. These findings are similar to Demko and Geerts (2010) who showed that mass convergence may sustain and facilitate orographic convection. The transition to divergent flow soon after deep convection can be induced by cold-air outflow.

The sensitivity studies with two modifications (namelist switch to lexpcor=.False. and a new aerosol climatology after Tegen et al. (1997)) in the model setup showed an improved simulation of SWin leading to a good representation of NR. This is in agreement with studies from Hohenegger and Vidale (2005) and Zubler et al. (2011) who showed that the underestimation of SWin results from a too large aerosol content over southern Europe. Despite the improved peak of SWin, the morning and evening

SWin was still overestimated. However, the influence of this improved SWin on the heating of the valley atmosphere and hence the pressure difference was small. Nevertheless an impact on precipitation rate is visible. Both modifications contributed to an earlier onset of precipitation, an earlier peak and a decreased nighttime precipitation amount.

Some further deficits in the model runs could be adressed: The overestimation of SWin in the morning and evening hours could come from a neglect of topographic shading. With enhanced model resolution this effect should be taken into account which will probably lead to an even better representation of SWin (Buzzi, 2008). This could also improve the onset and decay of the different parameters (e.g. anabatic wind, pressure gradient).
Though the difference between the CRMs is overall small some variations are visible. One of this is the partitioning of sensible and latent heat flux. The surface properties should be identical between both runs since a nearest neighbour interpolation was used in calculating the O(1 km)-run surface properties from the O(2 km)-run surface properties. Hence the difference could come from a different elevation of the grid-point and should be investigated further.
The overestimation of pressure gradient in the convection-parameterizing simulation which was not in phase with other parameters needed to be studied further. This could probably be done with an extended validation of pressure gradient using the Alpine polygon rather than this six selected valleys.
The persistence high cloud cover in all three model runs is remarkable and needs to be analysed further. With the two modelling sensitivity runs the different cloud types should be also investigated probably leading to better results and more insights in the interaction between Alpine pumping and deep convection could be gained.

A. “Valley-volume calculations”

Model	*maximal altitude*	*volume at ztop=1000m*	*volume at ztop=1500m*	*volume at ztop=2000m*	*volume at ztop=2500m*	*volume at ztop=3000m*
SU1	4072.27m	$1.54*10^4$ km^3	$4.80*10^4$ km^3	$9.76*10^4$ km^3	$1.61*10^5$ km^3	$2.32*10^5$ km^3
SU2	3935.84m	$1.43*10^4$ km^3	$4.67*10^4$ km^3	$9.66*10^4$ km^3	$1.60*10^5$ km^3	$2.31*10^5$ km^3
SU7	3138.54m	$1.12*10^4$ km^3	$4.22*10^4$ km^3	$9.25*10^4$ km^3	$1.57*10^5$ km^3	$2.29*10^5$ km^3

Table A.1.: ”Valley-volume calculations“ for the different model runs and for different z-tops for the Alpine arc as showed in Fig 3.1. Additionally the maximum altitude in the runs is listed.

B. Anabatic valley wind

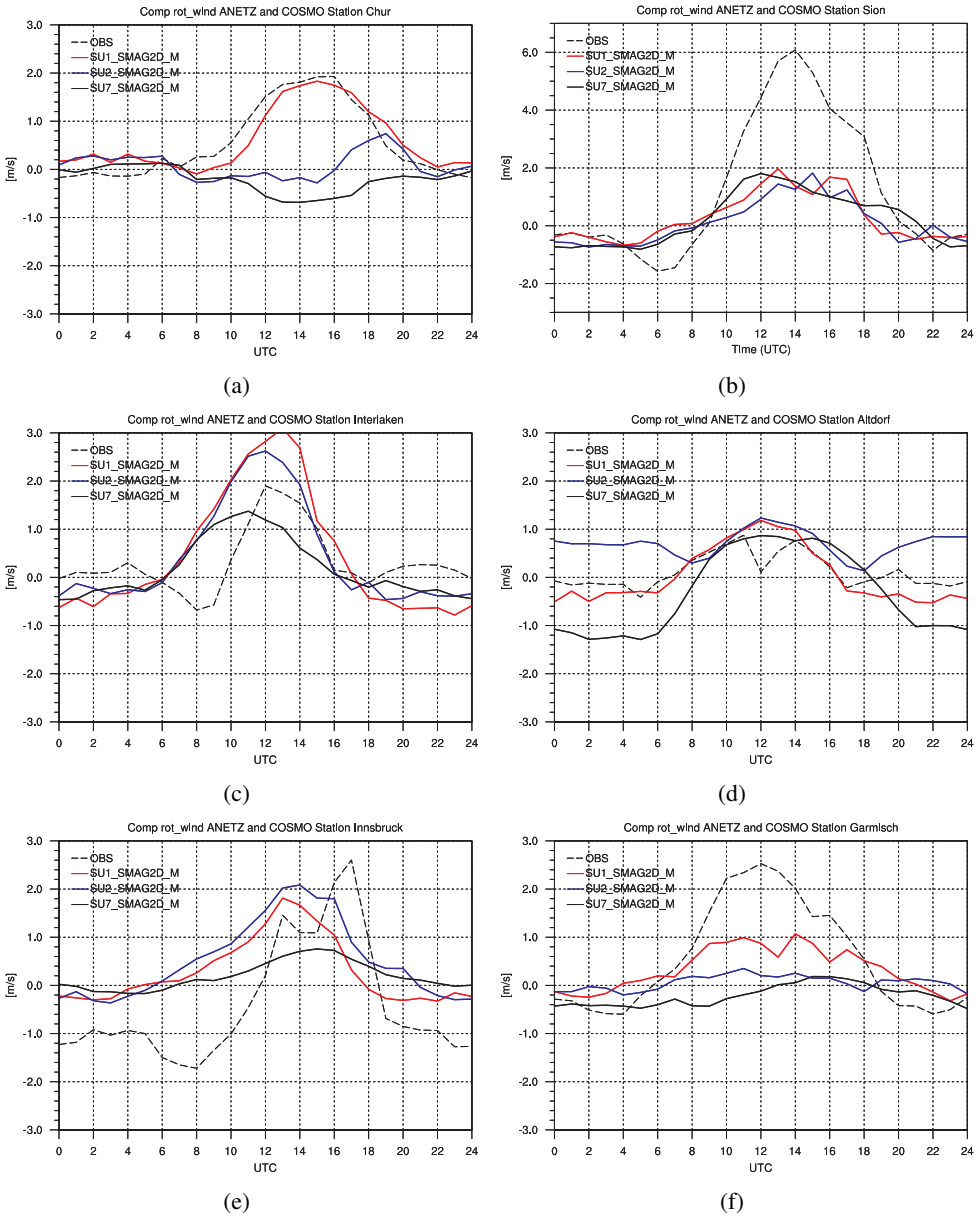

Figure B.1.: Diurnal cycle of anabatic valley wind (m s^{-1}) in the selected six valleys for the model runs (SU1: red, SU2: blue and SU7: solid, black) and observations (dashed, black). These six valleys were used for the calculation of the mean averaged cycle of anabatic valley wind showed in Fig. 4.1a.

C. Pressure difference

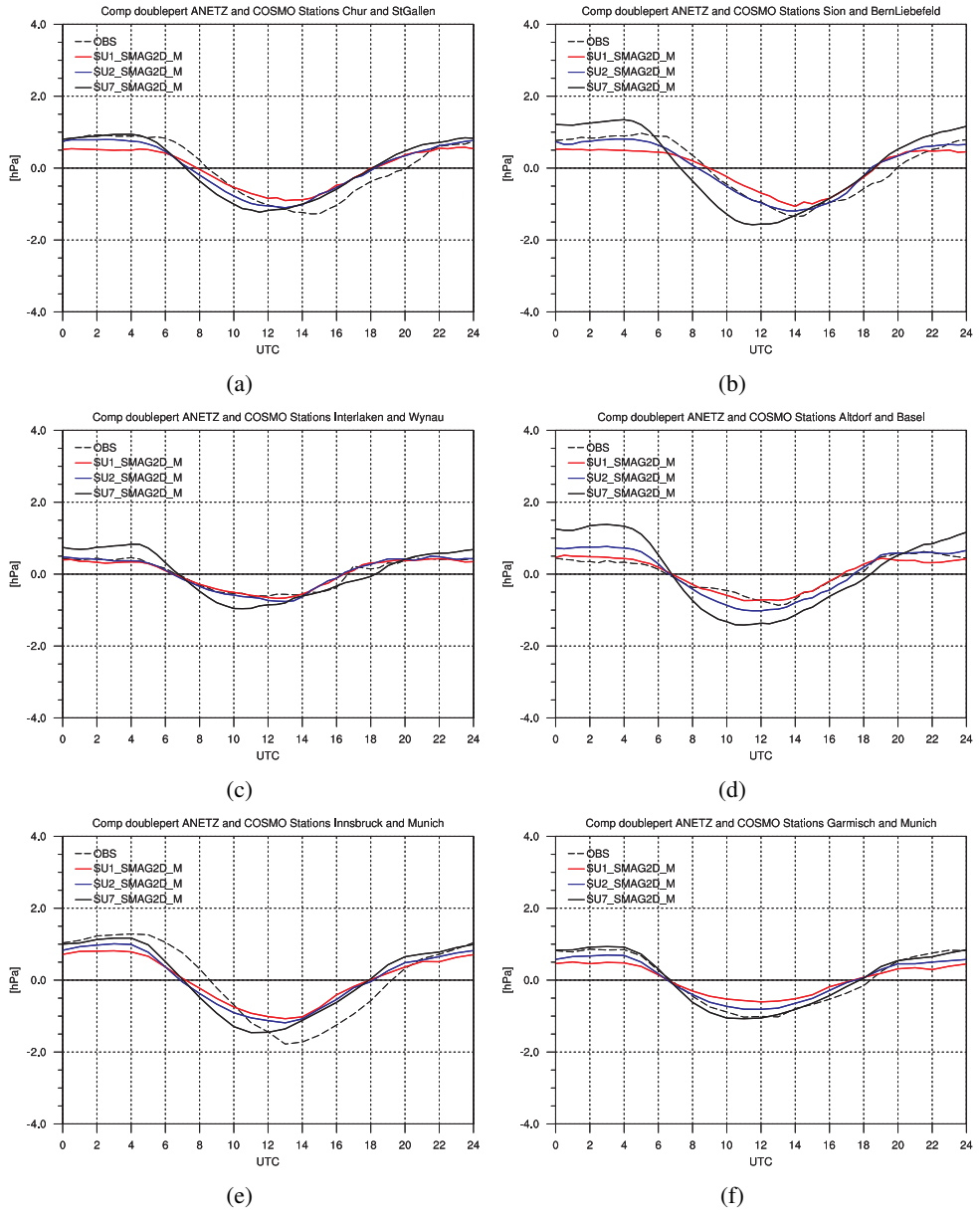

Figure C.1.: Diurnal cycle of pressure difference (hPa) in the selected six valleys for the model runs (SU1: red, SU2: blue and SU7: solid, black) and observations (dashed, black). These six valleys were used for the calculation of the mean averaged cycle of pressure difference showed in Fig. 4.4b.

D. Potential temperature perturbations

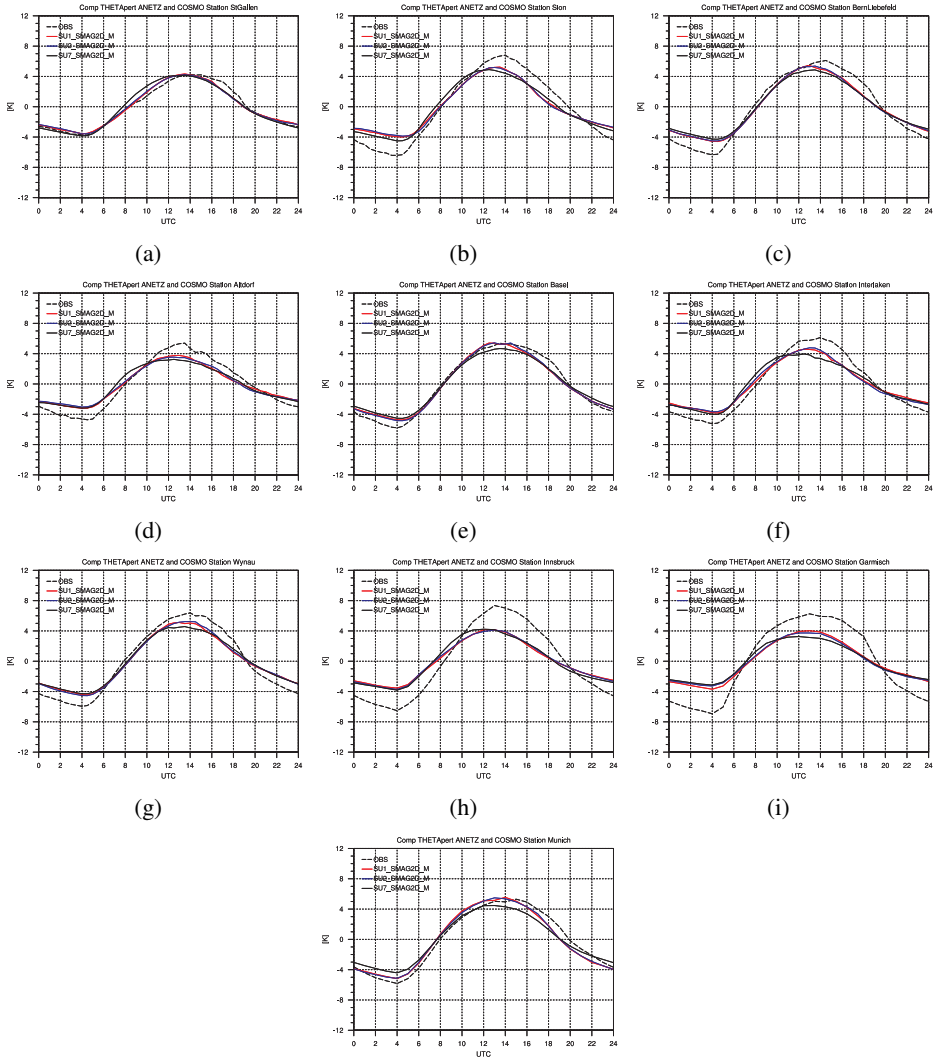

Figure D.1.: Diurnal cycle of potential temperature perturbations (K) in the selected valley and plain stations, respectively. The model runs (SU1 red, SU2 blue and SU7 black, solid) are compared to the observations (dashed, black). This data was used for the calculation of the mean averaged cycle of potential temperature perturbations showed in Fig. 4.4a.

E. Radiation

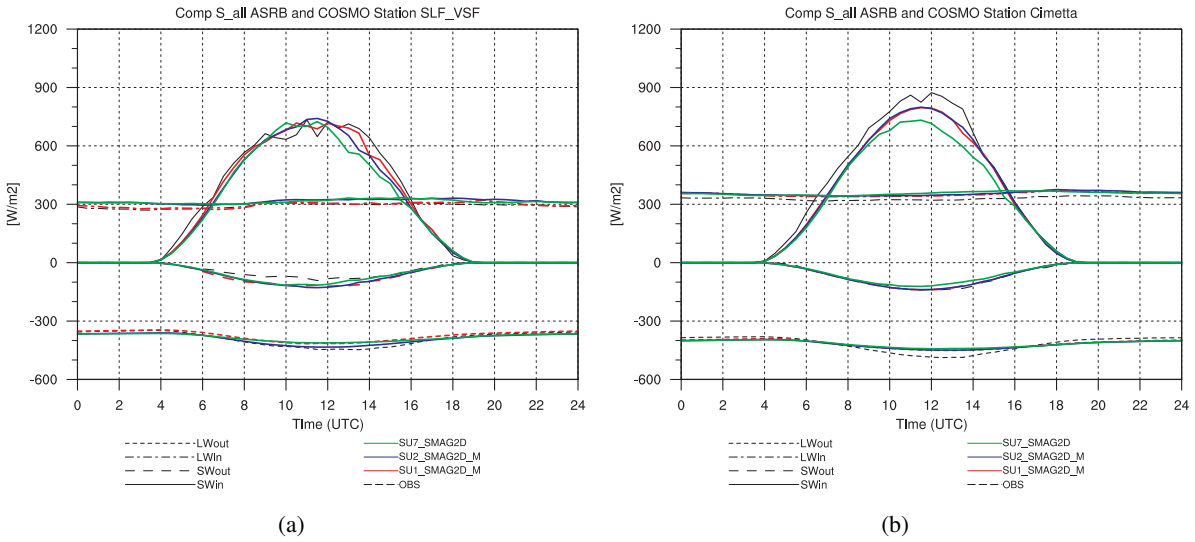

(a) (b)

Figure E.1.: Diurnal cycle of radiation balance for ASRB station (a) Versuchsfeld SLF and (b) Cimetta averaged over the whole month. Energy balance components are shown from (black) observations and (SU1 red, SU2 blue and SU7 green) simulations.

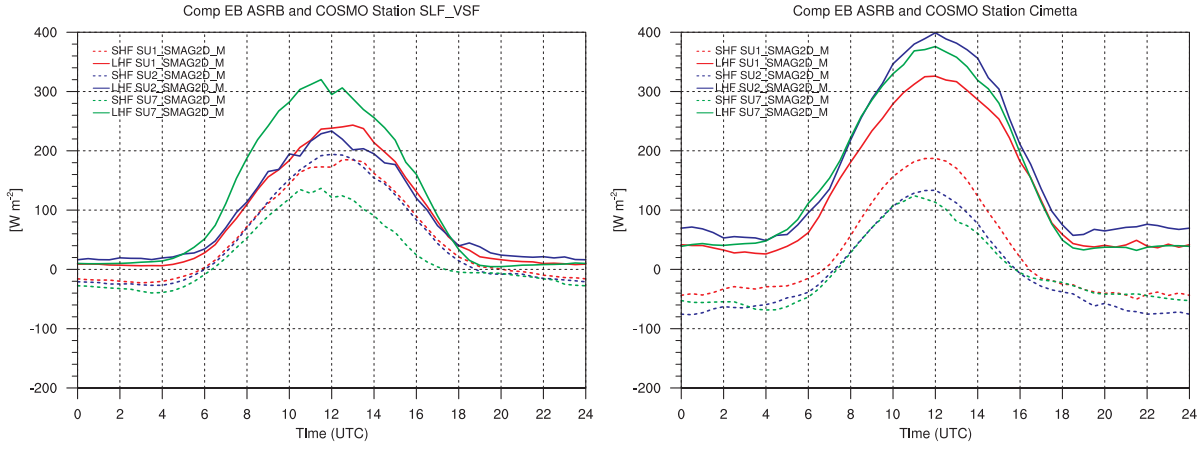

(a) (b)

Figure E.2.: Partitioning of the available energy in sensible (SHF) and latent (LHF) heat flux (W m^{-2}) for ASRB station (a) Versuchsfeld SLF and (b) Cimetta averaged for the whole July 2006. SU1 in red, SU2 in blue and SU7 in green. No observations are available.

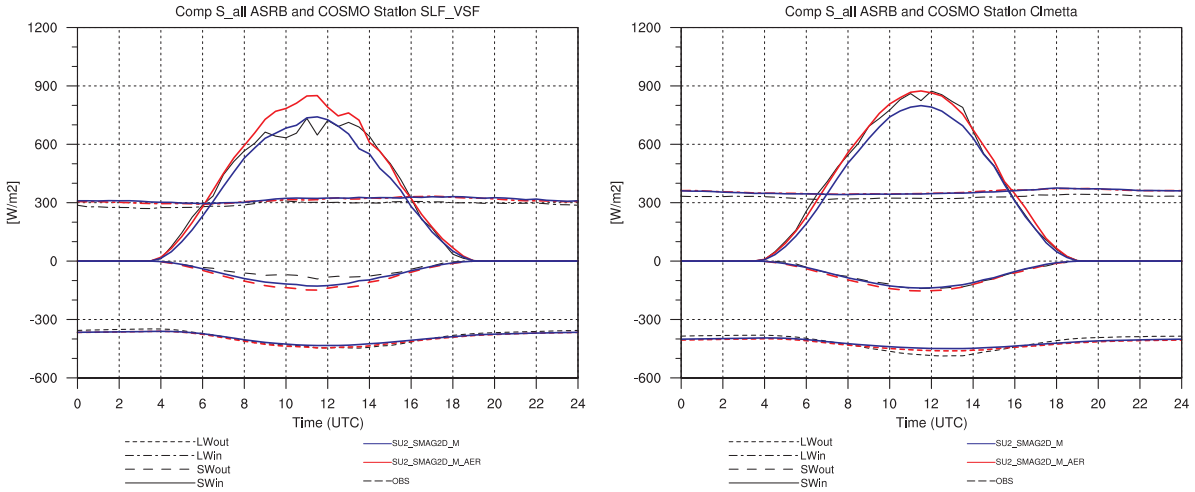

(a) (b)

Figure E.3.: Same as Fig. E.1, but for simulation SU2 and SU2_AER.

F. Pressure difference SU2 and SU2_AER

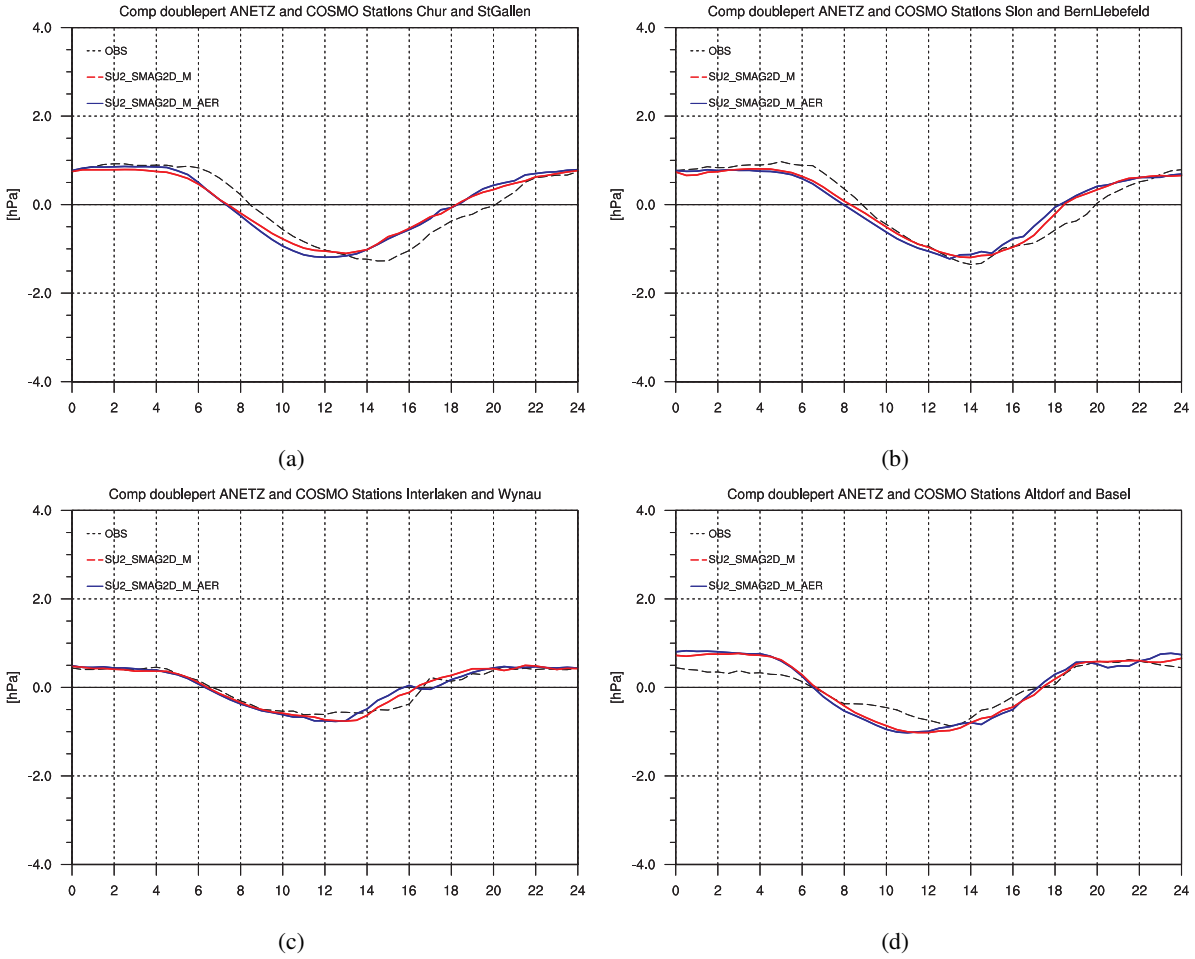

Figure F.1.: Same as Fig. C.1 but for simulations SU2 and SU2_AER and only four valleys.

G. Potential temperature perturbations SU2 and SU2_AER

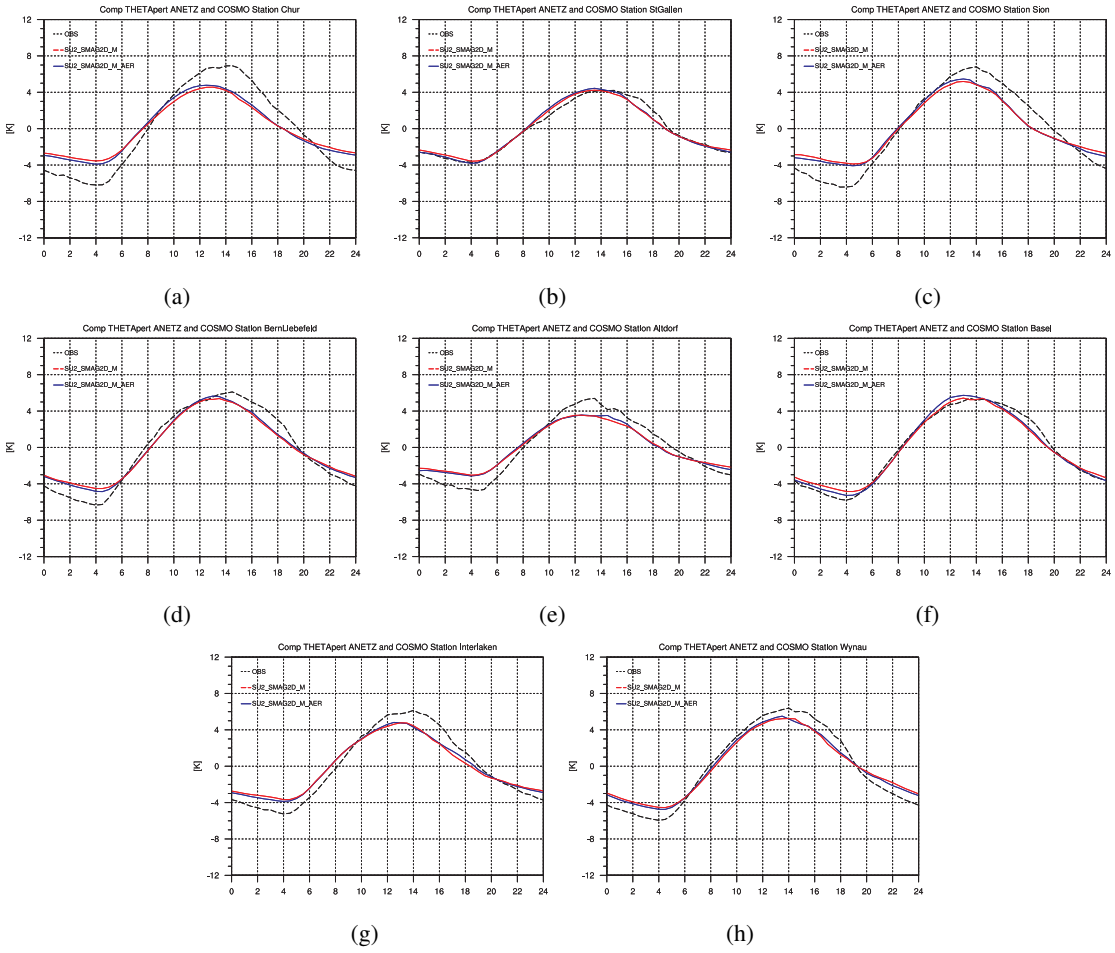

Figure G.1.: Same as Fig. D.1 but for simulations SU2 and SU2_AER and only for eight stations.

H. Radiosounding Payerne 1200Z 14 July 2006

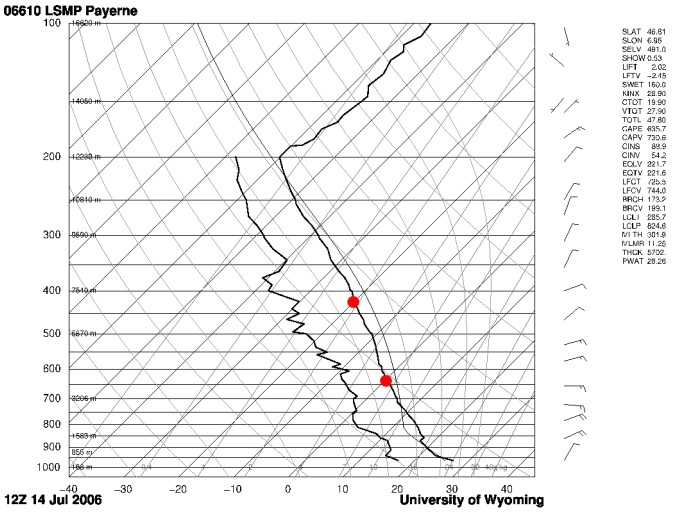

Figure H.1.: Radiosounding Payerne 1200Z 14 July 2006 used for the detection of the cloud height. The red points gives the limit of mid-level clouds -20°C < BT < 0°C which are located therefore approximately between 4000 m and 7000 m when assuming black-body emissivity. These height are approximately the same as used in synoptic weather classification (Ahrens, 1994) and therefore used for the classification of cloud types.

Acknowledgments

First of all I would like to thank Wolfgang Langhans for his encouraging and helpful supervision of this thesis. Without his great support and his interest on this subject the thesis would not make this good progress. He always took time for me despite his fully schedule, answered all my questions with patience and solved all my problems immediately.
A thank you goes to Jürg Schmidli for his helpful discussions and his critical and constructive remarks regarding my analysis. His knowledge of valley-wind systems was the driving force behind this thesis.
I would like to thank Christoph Schär for giving me the possibility to work on this master thesis, for his interests on my results and for the ideas concerning the course of this thesis. Thank you as well to Dani Lüthi for his technical support.
Thanks to MeteoSwiss, especially Tanja Weusthoff and Rolf Philipona for providing most of the observational data and Reto Stöckli for his script reading EUMETSAT data.

A big thank you goes to Alex, Nicolas, Paul, Yves and all other students in workplace D28.2 for the great working atmosphere, the helpful technical and scientific support, the friendly discussions and the great time also beside this thesis.

Thanks as well to my parents and my sister for their steady support concerning my plans and ideas. And thank you, Fabian, for the motivation, support, helpfulness during this thesis and for everything else!

Bibliography

Ackermann, A. 1996. Global satellite observations of negative brightness temperature differences between 11 and 6.7mikrom. *J. Atmos. Sci.* **53**, 2303–2812.

Ahrens, C. 1994. *Meteorology today: an introduction to weather, climate and environment*. West Pub.

Bedka, K., J. Brunner, R. Dworak, W. Feltz, J. Otkin, and T. Greenwald. 2010. Objective satellite-based detection of overshooting tops using infrared window channel brightness temperature gradients. *J. Appl. Meteor.* **49**, 181–201.

Bryan, G., J. Wyngaard, and J. Fritsch. 2003. Resolution requirements for the simulation of deep moist convection. *Mon. Wea. Rev.* **131**, 2394–2416.

Buzzi, M. 2008. *Challenges in operational numerical prediction at high resolution in complex terrain*. PhD thesis. Dissertation submitted to the Swiss Federal Institute of Technology, Zürich.

Christensen, J., and O. Christensen. 2003. Climate modelling: severe summertime flooding in Europe. *Nature* **421**, 805–806.

Defant, F. 1949. Zur Theorie der Hangwinde, nebst Bemerkungen zur Theorie der Berg- und Talwinde. *Arch. Meteor. Geophys. Bioklim.* **A1**, 421–450.

Demko, J., and B. Geerts. 2010. A numerical study of evolving convective boundary layer and orographic circulation around the Santa Catalina Mountains in Arizona. Part I: Circulation without deep convection. *Mon. Wea. Rev.* **138**, 1902–1922.

Demko, J., B. Geerts, and Q. Miao. 2009. Boundary layer transport and cumulus development over a heated mountain: an observational study. *Mon. Wea. Rev.* **137**, 447–468.

Doms, G., and J. Förstner. 2004. Development of a kilometer-scale NWP-System LMK. *COSMO Newsletter* Pp. 159–167.

Frei, C., and C. Schär. 1998. A precipitation climatology of the Alps from high-resolution rain-gauge observations. *Int. J. Climatol.* **18**, 879–900.

Frei, C., R. Schöll, S. Fukutome, J. Schmidli, and P. Vidale. 2006. Future change of precipitation extremes in Europe: Intercomparison of scenarios from regional climate models. *J. Geophys. Res* **111**, D06105.

Geerts, B., Q. Miao, and J. Demko. 2008. Pressure perturbations and upslope flow over a heated, isolated mountain. *Mon. Wea. Rev.* **136**, 4272–4288.

Germann, U., G. Galli, M. Boscacci, and M. Bolliger. 2006. Radar precipitation measurement in a mountainous region. *Quart. J. Roy. Meteorol. Soc.* **132**, 1669–1692.

Hohenegger, C., and P. Vidale. 2005. Sensitivity of the European climate to aerosol forcing as simulated with a regional climate model. *J. Geophys. Res.* **110**, doi:10.1029/2004JD005,335.

Hohenegger, C., P. Brockhaus, and C. Schär. 2008. Towards climate simulations at cloud-resolving scales. *Meteor. Z.* **17**, 383–394.

Keil, C., A. Taggerner, and T. Reinhardt. 2006. Synthetic satellite imagery in the Lokal-Modell. *Atmospheric Research* **82**, 19–25.

Langhans, W., J. Schmidli, and C. Schär. 2011. Mesoscale impacts of explicit numerical diffusion in a convection-permitting model. *submitted*.

Lugauer, M., and P. Winkler. 2005. Thermal circulation in South Bavaria - climatology and synoptic aspects. *Meteor. Z.* **14**, 15–30.

Lugauer, M., H. Berresheim, U. Corsmeier, A. Dabas, W. Dyck, S. Emeis, J. Egger, T. Fehr, F. Fiedler, C. Freuer, L. Gantner, S. Gilge, B. Heese, M. Hornsteiner, H. Höller, G. Jakobi, W. Junkermann, N. Kalthoff, U. Kaminski, M. Kirchner, H. Krämer, P. Köhler, C. Kottmeier, B. Luksch, H. Ott, C. Plass-Dülmer, O. Reitebuch, M. Tagliazucca, T. Trickl, S. Vogt, and P. Winkler. 2003. An overview of the VERTIKATOR project and results of Alpine pumping. *Ext. Abstr. Vol. A, Intern. Conf. Alpine Meteorol./MAP-meeting* Pp. 19.–23.5.2003, Brig (CH), 129–132.

Marty, C., R. Philipona, C. Frölich, and A. Ohmura. 2002. Altitude dependence of surface radiation fluxes and cloud forcing in the alps: results from the alpine surface radiation budget network. *Theor. Appl. Climatol.* **72**, 137–155.

MeteoSchweiz 2006. Juli 2006: Klimatologisch ein extremer Monat.. Pp. (Available online at http://www.meteoschweiz.admin.ch/web/de/wetter/wetterereignisse/juli_2006_erste_bilanz.html).

Rampanelli, G., D. Zardi, and R. Rotunno. 2004. Mechanism of up-valley winds. *J. Atmos. Sci.* **61**, 3097–3111.

Raschendorfer, M. 2001. The new turbulence parameterization of LM. Tech. rep.. *COSMO news-letter* **1**, 90–98, (available from http://www.cosmo–model.org).

Rotach, M., and D. Zardi. 2007. On the boundary-layer structure over highly complex terrain: Key findings from MAP. *Quart. J. Roy. Meteor. Soc.* **133**, 937–948.

Schmetz, J., A. Tjemkes, M. Gube, and L. van de Berg. 1997. Monitoring deep convection and convective overshooting with Meteosat. *Adv. Space Res.* **19**, 433–441.

Schmetz, J., P. Pili, S. Tjemkes, D. Just, K. Kerkmann, S. Rota, and A. Ratier. 2002. An introduction to Meteosat Second Generation (MSG). *Bulletin of the American Meteorological Society* **83**, 977–922.

Schmidli, J., and R. Rotunno. 2010. Mechanism of along-valley winds and heat exchange over mountainous terrain. *J. Atmos. Sci.* **67**, 3033–3047.

Smagorinsky, J. 1963. General circulation experiments with the primitive equations. *Mon. Wea. Rev.* **91**, 99–164.

Solomon, S., D. Qin, M. Manning, Z. Chen, M. Marquis, K. Averyt, M. Tignor, and H. Miller. 2007. IPCC, 2007: Climate Change 2007: The physical science basis. Contribution of working group I to the fourth assessment report of the intergovernmental panel on climate change.

Steinacker, R. 1984. Area-height distribution of a valley and its relation to the valley wind. *Contrib. Atmos. Phys.* **57**, 64–71.

Steppler, J., G. Doms, U. Schättler, H. Bitzer, A. Gassman, U. Damrath, and G. Gregoric. 2003. Meso-gamma scale forecasts using the nonhydrostatic model LM. *Meteorol Atmos Phys* **82**, 75–96.

Tanré, D., J. Geleyn, and J. Slingo. 1984. First results of the introduction of an advanced aerosol-radiation interaction in ECMWF low resolution global model, in Aerosols and Their Climate Effects, edited by H. Gerber and A. Deepak, pp. 133-177, A. Deepak, Hampton, Va.

Tegen, I., P. Hollrig, M. Chin, I. Fung, D. Jacob, and J. Penner. 1997. Contribution of different aerosol species to the global aerosol extinction optical thickness: Estimates from model results. *J. Geophys. Res* **102**, 23,895–23,915.

Tiedtke, M. 1989. A comprehensive mass flux scheme for cumulus parameterization in large-scale models. *Mon. Wea. Rev.* **117**, 1779–1800.

Trentmann, J., C. Keil, M. Salzmann, C. Barthlott, H.-S. Bauer, T. Schwitalla, M. G. Lawrence, D. Leuenberger, V. Wulfmeyer, U. Corsmeier, C. Kottmeier, and H. Wernli. 2009. Multi-model simulations of a convective situation in low-mountain terrain in central Europe. *Meteor. Atmos. Phys.* **103**, 95–103.

Weissmann, M., F. Braun, L. Gantner, G. Mayr, S. Rham, and O. Reitebuch. 2005. The alpine mountain-plain circulation: Airborne doppler lidar measurements and numerical simulations. *Mon. Wea. Rev.* **133**, 3095–3109.

Whiteman, C. 1990. Observations of thermally developed wind systems in mountainous terrain. Chapter 2 in Atmopsheric processes over complex terrain.. *Meteor. Monogr.* **23**, 5–42.

Wüest, M., C. Frei, A. Altenhoff, M. Hagen, L. M., and C. Schär. 2009. A gridded hourly precipitation dataset for Switzerland using rain-gauge analysis and radar-based disaggregation. *Int. J. Climatol.* **100**, 3019–3032.

Zubler, E., U. Lohmann, D. Lüthi, and C. Schär. 2011. Impact of an improved aerosol climatology in a regional climate model over Europe. *submitted*.